

# Ecohydrological Model for Grasslands Lacking Historical Measurements II: Confluence Simulations Based on Dynamic Channel Parameters

Mingyang Li<sup>1</sup>, Tingxi Liu<sup>1</sup>, Limin Duan<sup>1</sup>, Long Ma<sup>1</sup>, Qiusheng Wu<sup>2</sup>, Yixuan Wang<sup>1</sup>, Guoqiang Wang<sup>3</sup>, Huimin Lei<sup>4</sup>, Vijay P Singh<sup>5</sup>, Sinan Wang<sup>6</sup>, and Junfang Liu<sup>3</sup>

<sup>1</sup>Inner Mongolia Agricultural University

<sup>2</sup>University of Tennessee at Knoxville

<sup>3</sup>Beijing Normal University

<sup>4</sup>Tsinghua University

<sup>5</sup>Texas A&M University

<sup>6</sup>Inner Mongolia Agricultural University

November 24, 2022

## Abstract

Technology has greatly promoted ecohydrological model development, but runoff generation and confluence simulations have fallen behind in ecohydrological model development due to limited innovations. To fully understand ecohydrological processes and accurately describe the coupling between ecological and hydrological processes, a distributed ecohydrological model was constructed by integrating multisource information into MYEH. We mainly describe runoff generation and convergence modules. Based on the improved HBV model and degree-3 hour factor method, runoff generation and snow routines were constructed for semiarid grassland basins. In view of meandering and variable steppe river channels and steep hydrological relief characteristics, a confluence module was constructed; the 1-km bend radius equivalent concept was innovatively proposed to unify river channel bend degrees. The daily runoff simulation validation results obtained using two datasets were  $R^2=0.947$  and  $0.932$ ,  $NSE=0.945$  and  $0.905$ , and  $KGE=0.029$  and  $0.261$ . In the 3-hour flood simulations, the MYEH model could better restore small long-distance water flows than the confluence method that did not consider actual river lengths or bend energy losses; the MYEH model more accurately simulated the flood peak arrival time than the confluence method that did not consider overflow. The simulated mainstream overflow frequency increased by 0.84/10 years, and significant interaction periods of 10 to 13 years occurred with local precipitation, ecological status and global climate change. An approximately 2-year lag occurred in the global climate change response. This study helps us further understand and reveal the ecohydrological processes of steppe rivers in semiarid regions.

1        **Ecohydrological Model for Grasslands Lacking Historical Measurements II:**

2                    **Confluence Simulations Based on Dynamic Channel Parameters**

3        **Mingyang Li<sup>1</sup>, Tingxi Liu<sup>1\*</sup>, Limin Duan<sup>1</sup>, Long Ma<sup>1</sup>, Qiusheng Wu<sup>2</sup>, Yixuan Wang<sup>1</sup>,**  
4        **Guoqiang Wang<sup>3</sup>, Huimin Lei<sup>4</sup>, Vijay Singh<sup>5</sup>, Sinan Wang<sup>1</sup>, Junfang Liu<sup>3</sup>**

5        (<sup>1</sup> *Inner Mongolia Water Resource Protection and Utilization Key Laboratory; Water Conservancy and Civil*  
6        *Engineering College, Inner Mongolia Agricultural University, Hohhot 010018, China;*

7        <sup>2</sup> *Department of Geography, University of Tennessee, Knoxville, TN 37996-0925, USA;*

8        <sup>3</sup> *College of Water Sciences, Beijing Normal University, Beijing 100875, China;*

9        <sup>4</sup> *State Key Laboratory of Hydrosience and Engineering, Department of Hydraulic Engineering,*  
10        *Tsinghua University, Beijing 100084, China;*

11        <sup>5</sup> *Department of Biological and Agricultural Engineering & Zachry Department of Civil Engineering, Texas*  
12        *A&M University, College Station, TX 77843, USA)*

13  
14        **Key Points:**

- 15        ● Using actual river length, bend radius equivalent and overflow data helps improve the  
16        steppe river confluence process
- 17        ● The MYEH confluence module simulates the river diversion effect on the confluence  
18        before and after a flood
- 19        ● Precipitation, ecological status and climate change significantly interact with OFN, and  
20        the overflow response to climate has a 2-year lag
- 21

## 22 Abstract

23 Technology has greatly promoted ecohydrological model development, but runoff generation  
24 and confluence simulations have fallen behind in ecohydrological model development due to  
25 limited innovations. To fully understand ecohydrological processes and accurately describe the  
26 coupling between ecological and hydrological processes, a distributed ecohydrological model  
27 was constructed by integrating multisource information into MY ecohydrological (MYEH)  
28 model. We mainly describe runoff generation and convergence modules. Based on the  
29 improved HBV model and degree-3 hour factor method, runoff generation and snow routines  
30 were constructed for semiarid grassland basins. In view of meandering and variable steppe  
31 river channels and steep hydrological relief characteristics, a confluence module was  
32 constructed; the 1-km bend radius equivalent concept was innovatively proposed to unify river  
33 channel bend degrees. The daily runoff simulation validation results obtained using two  
34 datasets were  $R^2=0.947$  and  $0.932$ ,  $NSE=0.945$  and  $0.905$ , and  $KGE=0.029$  and  $0.261$ . In the  
35 3-hour flood simulations, the MYEH model could better restore small long-distance water  
36 flows than the confluence method that did not consider actual river lengths or bend energy  
37 losses; the MYEH model more accurately simulated the flood peak arrival time than the  
38 confluence method that did not consider overflow. The simulated mainstream overflow  
39 frequency increased by 0.84/10 years, and significant interaction periods of 10 to 13 years  
40 occurred with local precipitation, ecological status and global climate change. An  
41 approximately 2-year lag occurred in the global climate change response. This study helps us  
42 further understand and reveal the ecohydrological processes of steppe rivers in semiarid regions.

43

## 44 1 Introduction

45 An ecohydrological model is a generalized expression of ecohydrological phenomena  
46 and processes created using mathematical language and physical processes (Svoray et al.,  
47 2015); these models help researchers describe the interactions between ecological and  
48 hydrological processes (Geng et al., 2020) and reveal the succession of ecological patterns and  
49 the synergy mechanisms involved in the hydrological cycle as it relates to ecological processes  
50 (Wu et al., 2021a). The results of many studies based on model designs and improvements have  
51 shown that ecohydrological models exhibit better simulation performances at their respective  
52 target scales and ecosystems (Sun et al., 2020; Yan et al., 2021). China's temperate grassland  
53 area covers a region spanning  $1.68 \times 10^6$  km<sup>2</sup>, accounting for 11.2% of the total global  
54 grassland area, concentrated in the semihumid and semiarid areas of northeastern China (Wu  
55 et al., 2021b). Grassland ecosystems have suffered degradation due to climate change,  
56 excessive grazing, and irrational development (Goenster-Jordan et al., 2021; Yin et al., 2018).  
57 Suitable models have been established based on ecohydrology for ecosystems with abundant  
58 water in humid and subhumid areas (Zha et al., 2020), alpine mountains (Tong et al., 2021),  
59 wetlands (Lou et al., 2019), and deserts (Yin et al., 2021). However, ecohydrological models  
60 that are specifically applicable to arid and semiarid steppe regions have rarely been reported.  
61 Semiarid grassland ecosystems are relatively barren, although their corresponding vegetation  
62 communities are rich and diverse. The evolution of ecohydrological processes, coupling  
63 mechanisms, and mutual feedback effects have strong regional characteristics in these regions

64 that cannot be accurately described with existing models. Therefore, in the context of global  
65 ecological governance and protection, developing and debugging an ecohydrological model  
66 that is specifically applicable to arid and semiarid steppe regions is of great scientific  
67 significance (Ma et al., 2019).

68 Under the action of gravity, water from precipitation or icemelt flows into river  
69 networks from ground-surface and underground sources; the water that flows out of the basin  
70 outlet section becomes runoff (Betson, 1964; Cadle et al., 1987; Chang & Yeh, 2018; Poiani &  
71 Johnson, 1993; Young & Liu, 2015; Zhang & Singh, 2014). The runoff formation process can  
72 be generalized into runoff-generating and confluence processes (Gentry & Lopez-Parodi, 1980;  
73 Muzik, 1992; Xiong & Guo, 2004). Runoff simulations involve rainfall loss simulations and  
74 can be divided into two parts: evaporation and infiltration (processes such as plant interception  
75 and hollow depressions filling with dammed-up water resulting in the loss of water into the  
76 atmosphere through evaporation or the eventual infiltration process into the soil; here, these  
77 processes are not listed separately) (Asdak et al., 1998; David et al., 2005; Jakeman &  
78 Hornberger, 1993; Maniquiz et al., 2012). Confluence analyses include the calculation of  
79 confluence within a given hydrological response unit and the calculation of river confluence  
80 (flood calculus) (Moore & Grayson, 1991; Osborn & Lane, 1969; Vassova, 2013; Wendi et al.,  
81 2019). At present, a large number of studies have been carried out on evapotranspiration and  
82 infiltration in combination with the rapid development of remote sensing technologies and  
83 easily operated field experiments (den Besten et al., 2021; Dunne & Black, 1970; Li et al., 2020;  
84 Qiu et al., 2006; Yang et al., 2015). Due to the difficulty of obtaining spatially and temporally  
85 continuous confluence process observations, the many influencing factors, and the difficulty  
86 of solving partial differential equations of flood waves (David et al., 2019; Hassini & Guo,  
87 2017; Yamanaka & Ma, 2017), both the understanding of the convergence process and the  
88 related research are far from sufficient (Hood et al., 2007; Song et al., 2020; Tanaka et al., 2005;  
89 Zoccatelli et al., 2019); these inadequacies are even more obvious in semiarid steppe  
90 watersheds where rivers meander and are changeable and floods rise and fall steeply.

91 Two major equations are used to calculate unsteady flow in open channels, the  
92 continuity equation and momentum equation; these equations are the basis of the Saint Venant  
93 equations (Carraro et al., 2018; Ding & Wang, 2005; Strelkoff, 1970; Wang et al., 2003). By  
94 simplifying the continuity equation to the water balance equation and the dynamic equation to  
95 the water tank storage relationship in the analyzed reach, the widely used Muskingum method  
96 can be deduced for the confluence calculation (Al-Humoud & Esen, 2006; Bozorg-Haddad et  
97 al., 2015; Choudhury et al., 2002; Gill, 1978; Tung, 1985). The key to the application of the  
98 Muskingum method is determining how to reasonably calculate the  $k$  and  $x$  parameters, that is,  
99 the average propagation time of the analyzed reach and the weight used to measure the effects  
100 of inflow and outflow on river storage (Al-Humoud & Esen, 2006; Bozorg-Haddad et al., 2019;  
101 David et al., 2015). However, traditionally utilized hydrological variables, such as the average  
102 propagation time, are no longer applicable to today's severely degraded steppe rivers. The  
103 current models have difficulties when (or are even incapable of) simulating the confluence  
104 processes of steppe rivers due to river characteristics such as instantaneous and rapidly  
105 changing discharge, sandy soils with low water-storage capacities, and the irregular and easy  
106 migration of river patterns (Birkhead & James, 2002; Bozorg-Haddad et al., 2019; Hamedi et  
107 al., 2016).

108 In view of the above existing problems and river characteristics, we constructed a  
109 runoff-generating and confluence module in the MY ecohydrological (MYEH) model (Figure  
110 1). We improved the Hydrologiska Byrans Vattenbalansavdelning (HBV) model, which is  
111 applicable as a runoff-generating model in arid and semiarid regions, used the degree-3 hour  
112 factor instead of the degree-day factor to calculate the snowmelt and accumulation processes,  
113 and innovatively proposed a river network confluence module based on dynamic river length,  
114 river bend, 3-hour scale unit flood peak duration, and river overflow during flood transit  
115 information. Specifically, our objective was to (1) dynamically simulate and depict river flows,  
116 river types and other parameter change processes in grasslands; (2) explore and verify the  
117 applicability of the MYEH model to different input data sources and determine and explain the  
118 physical meaning of each process parameter; (3) compare the advancement of the convergence  
119 module with the existing convergence calculation method and explore the resulting space for  
120 improvement opportunities; (4) and simulate and explore the responses of river overflows to  
121 regional meteorological and ecological conditions and global climate change to further  
122 understand and reveal the unique ecohydrological processes of typical steppe regions.

123

124 **Figure 1.** Schematic diagram of natural processes such as the flow convergence, actual river  
125 lengths, and channel turns of grassland rivers. Note: The river network shown in the figure  
126 does not correspond to the real modelled river network resolution.

127

## 128 2 Method

### 129 2.1 Study area

130 The study area is located in the Xilin River basin (XRB) in the Inner Mongolia  
131 Autonomous Region, China (43°30'–44°4' N, 115°37'–117°30' E) and is characterized by a  
132 continental climate in the middle temperate zone. The annual average temperature in the study  
133 area is 2.6 °C, the annual evapotranspiration (ET) is significant, and sunshine is intense. Overall,  
134 the terrain is high in the southeast and low in the north, with elevations ranging from 977 to  
135 1620 m (Figure 2a). In the southeastern part of the study area, there is a multilevel platform  
136 with a high elevation and a high number of gullies. Many fixed dunes are distributed in the  
137 middle of the tributary and the mainstream region. Several of these dunes are semifixed with  
138 notable wind erosion. More than 90% of the vegetation is natural foliage, including *Leymus*  
139 *chinensis* Tzvel., *Stipa grandis* P. Smirn., and *Stipa krylovii* Roshev. A certain amount of  
140 *Achnatherum splendens* Nevski vegetation can be found in the degraded wetlands and  
141 surrounding valleys. Many shrubs, such as *Stipa baicalensis* Roshev. and *Caragana*  
142 *microphylla* Lam., can be found in the higher arid steppe regions. The desert landscape in the  
143 central part of the study area is mainly composed of *Ulmus pumila* Linn., whereas *Picea*  
144 *asperata* Mast. and *Betula platyphylla* Suk. are distributed in the northeast region.

145 According to incomplete statistics, historical measured data in the XRB are relatively  
146 scarce. Only one Chinese National Hydrological Station and one Chinese National  
147 Meteorological Station had been built in 1964; these stations are located in an urban area and  
148 thus have little significance in reflecting the meteorological conditions of the studied grasslands  
149 in the historical period. To more accurately monitor the hydrometeorological conditions in the

150 XRB, we set up 3 sets of automatic velocity and flow monitoring stations, 1 set of Bowen ratio  
 151 weather stations, 6 sets of automeasuring rain stations and 7 manual flow monitoring stations  
 152 in the research area. The specific location of each station can be seen in [Figure 2b](#) and [Table 1](#)  
 153 lists the specific station information.

154

155 **Figure 2.** Location, vegetation types (a), topography and stations (b) in the XRB. SBG: *S.*  
 156 *baicalensis* Roshev. grassland; LCG: *L. chinensis* (Trin.) Tzvel. grassland; SKG: *S. krylovii*  
 157 Roshev. grassland; SGG: *S. grandis* P.A. Smirn. grassland; ASG: *A. splendens* (Trin.) Nevski  
 158 grassland; CMG: *C. microphylla* Lam grassland; AFG: *Artemisia frigida* Willd. grassland;  
 159 PAG: *P. asperata* Mast. grassland; FSG: *Filifolium sibiricum* (L.) Kitam. grassland; and WCG:  
 160 weed community grassland.

161

162 **Table 1.** Information of measurement stations in the XRB.

163

## 164 2.2 Model

165 MYEH model is a bidirectional coupling eco-hydrological model for (but not limited  
 166 to) steppe inland river basins in arid and semi-arid regions, which is driven by meteorological  
 167 data and developed by Dr. Mingyang Li and Prof. Tingxi Liu. MY means “my”, which will be  
 168 released as open source and gradually optimized and updated to get more support from  
 169 researchers and better improve the model. The MYEH model mainly includes  
 170 evapotranspiration, runoff, confluence, grazing disturbance, carbon and nitrogen cycle, etc. It  
 171 absorbs the advantages of various existing ecological models, hydrological models, as well as  
 172 the framework and algorithm of eco-hydrological models.

173 The runoff generation and convergence processes are reflected in the MYEH model  
 174 with two modules: the simulation module (Sim module), which was improved based on the  
 175 hydrological model (HYMOD) and HBV models ([BERGSTRÖM, 1975](#); [Kollat et al., 2012](#);  
 176 [Moore, 2007](#); [Seibert, 2000](#)), and the self-developed flow confluence module (FLC module).  
 177 The function of the Sim module is to calculate the flow yield of each grid cell in the basin in  
 178 units of time using input data such as temperature, precipitation, actual evapotranspiration  
 179 (calculated by the Eva module in the MYEH model) and grid area data. The FLC module  
 180 calculates all grid-simulated runoff in the basin according to the river direction generated using  
 181 basin elevation, river width, river length, roughness and other characteristic data based on the  
 182 runoff yield and upstream inflow calculated by the Sim module. The Monte Carlo method is  
 183 used to calibrate the model; this method can not only eliminate any deviation in the calibration  
 184 process but can also obtain the optimal parameter set. [Table 2](#) lists the parameters, units and  
 185 rate-setting ranges used by the Sim and FLC modules.

186

187 **Figure 3.** (a) Schematic diagram of the MYEH model simulation (Sim) module; (b) schematic  
 188 diagram of the MYEH model flow confluence (FLC) module. The full names of the variables  
 189 shown in [Figure 3a](#) can be seen in [Table 2](#). DEM: digital elevation model; RS: remote sensing;

190 1-km RBRE: 1-km river bend radius equivalent; FTL: flow time length; FFTL: fixed flow time  
191 length; and RDacc: accumulated runoff depth.

192

193 **Table 2.** Summary of parameters used in the Sim module and FLC module within the MYEH  
194 model.

195

## 196 2.2.1 Sim module

197 The Sim module mainly includes the snow routine, soil moisture units and flow  
198 generation units (Figure 3a). We refer to the degree-day method concept holistically in this  
199 module (BERGSTRÖM, 1975). To adapt to the confluence time scale, the 3-hour unit is used  
200 to replace the number of days, and the model is improved to a degree-3 hour factor method to  
201 improve the simulation accuracy of the diurnal flow generation process. These processes are  
202 explained and described below.

203

### 204 2.2.1.1 Snow accumulation & melting routine

205 The snow routine is a subprogram used to describe the accumulation and ablation of  
206 snow, as water is fed into the soil moisture zone through these processes. We treat the snowmelt  
207 water in the soil in the same way as we treat rainfall, whereas snowfall on lakes is not treated  
208 using snowfall procedures because the pressure effect this snow has on lake ice has the same  
209 effect as rainfall on an ice-free lake (BERGSTRÖM, 1975).

210 The first step is to determine whether precipitation accumulates as snow or directly  
211 enters the soil moisture zone as liquid water. A physically correct snowmelt model should  
212 consider the entire energy balance of a snowpack, including consideration of sensible and latent  
213 heat fluxes, radiation, energy exchanges with the ground, the contribution of precipitation, and  
214 the thermal mass of snow itself (Kollat et al., 2012). In view of the uncertainty of the available  
215 data and the desire to avoid unreasonable complexity, we adopt the degree-3 hour factor  
216 method, representing an improvement from the degree-day factor method.

217 Temperature is selected as a representative index affecting snow melt. We set a  
218 temperature threshold parameter ( $T_s$ ) to judge the temperature boundary, whether precipitation  
219 falls in the form of rain or snow, and whether fallen snow accumulates or melts. Additionally,  
220 snowbanks are assumed to retain meltwater, which is expressed as a fraction of their total water  
221 storage in terms of the corresponding water holding capacity (CWH) of the snow parameter.  
222 Meltwater contained within a snowpack can also be refrozen according to the refreezing  
223 parameter (CFR), which is expressed as a fraction of the degree-3 hour factor (CFMAX). See  
224 Hamilton et al. (2000) for more details on the formula of the degree-daily snowfall module.

225

### 226 2.2.1.2 Soil moisture accounting routine

227 The soil water unit calculation performed in the Sim module uses the storage capacity  
228 distribution function of a given storage unit. In this module, the storage elements of the  
229 analyzed watershed are distributed according to the probability density function defined by the

230 maximum soil water storage and soil water storage distribution. The maximum soil water  
231 storage ( $C_{max}$ ) represents the maximum soil water storage capacity, while the shape parameter  
232 ( $BETA$ ) describes the degree of spatial variability in the soil water storage (Wagener et al.,  
233 2004).

234 In contrast from the process involved in HYMOD, in this study, the soil water storage  
235 evaporation rate is calculated using the entity views attachment (EVA) module in the MYEH  
236 model. After the evaporation fraction is removed, surplus rainfall and snowmelt are used to fill  
237 the soil water reserves, and excess rainfall is sent to the flow-producing unit. In addition, we  
238 define the soil water storage limit ( $LP$ ) when potential evaporation occurs. For soil water  
239 storage measurements between 0 and  $LP$ , the ratio of actual evaporation to potential  
240 evaporation changes linearly. For soil water storage measurements greater than or equal to  $LP$ ,  
241 the actual evaporation is equal to the potential evaporation.

242

### 243 2.2.1.3 Runoff generating routine

244 Similar to the process applied in the HBV model, the flow generating unit of the Sim  
245 module involves the conversion of excess rainfall from the soil moisture storage module to the  
246 runoff module. The excess rainfall and snowmelt remaining after evaporation, as well as the  
247 filled soil water stores, are channeled into an upper response reservoir ( $UZ$ ). Runoff is divided  
248 into three outlets from this upper response reservoir: near-surface flow, confluence and seepage  
249 to the base flow. The flows at these three outlets are defined by the near-surface flow regression  
250 coefficient ( $K_0$ ), middle flow regression coefficient ( $K_1$ ) and seepage rate ( $PERC$ ). The  
251 threshold parameter ( $L$ ) defines the runoff height at which near-surface flow occurs in the upper  
252 response reservoir. The runoff flowing into the lower response reservoir ( $LZ$ ) is released  
253 according to the base flow regression coefficient ( $K_2$ ). A triangular distribution ( $MaxBas$ ) is  
254 used to convert the runoff released from the reservoir from the top to the bottom, and finally,  
255 the runoff producing depth generated by the grid per unit time is obtained.

256

### 257 2.2.2 FLC module

258 The main work of the FLC module involves summarizing and calculating the runoff  
259 producing depth and upstream inflow of each grid cell in the studied basin in units of time  
260 according to the flow direction of the river; this work can be mainly divided into three units:  
261 inputs, process variable calculations and operation outputs (Figure 3b).

262

#### 263 2.2.2.1 FLC module input unit

264 The input unit mainly includes elevation data obtained by using a digital elevation  
265 model ( $DEM$ ) to calculate the grid flow direction and watershed boundaries, using remote  
266 sensing data to extract river features, and runoff producing depth time series calculated by the  
267 Sim module.

268 The flow direction is calculated by inputting the watershed boundaries and grid  $DEM$   
269 into the model. According to the extreme value selection principle of, we can obtain the flow

270 direction of the water in each grid cell in the analyzed watershed. While this method can be  
 271 used to solve most cases, when there are depressions, occlusive lakes or other unique terrains  
 272 in the basin, the flow direction can form a dead cycle that obviously cannot be satisfied by such  
 273 a calculation method. Different from the depression-filling tools of the ArcHydro or Soil and  
 274 Water Assessment Tool (SWAT) model, the idea constructed herein to solve such problems  
 275 involves initially setting up the outlet of the basin and then determining the flow path of each  
 276 grid cell to this established outlet. When the path is detected to enter a dead cycle, the module  
 277 determines the shape of the depression according to the cycle characteristics, looks for the  
 278 discharge mouth of the depression, and then directs the flow to the mainstream. Through high-  
 279 resolution remote sensing images and field measurement data, we extracted and prepared the  
 280 characteristic river quantitative data, including the actual river length, average river width, river  
 281 bend angle and radius, river roughness, slope and other factors inside each grid cell.

282

### 283 2.2.2.2 FLC module variable-processing unit

284 The variable-processing unit in the FLC module is mainly used to calculate the channel  
 285 state and hydraulic parameters of each grid cell during the flow generation period; this unit can  
 286 be used to debug and perform aggregation calculations at the output unit. At each calculation  
 287 step for each grid cell, we first calculate the river discharge, flow velocity and river depth using  
 288 the runoff depth and grid area:

$$289 \quad RD = Q\Delta t/1000A_G \quad (1)$$

$$290 \quad Q = A_S \times v = W_R \times H_R \times v \quad (2)$$

291 where  $RD$  is the runoff depth (mm);  $Q$  is the average flow discharge ( $\text{m}^3 \text{dt}^{-1}$ ) in units of time  
 292 ( $\Delta t$ );  $A_G$  is the grid area ( $\text{km}^2$ );  $A_S$  is the sectional area ( $\text{m}^2$ );  $v$  is the flow velocity; and  $W_R$   
 293 and  $H_R$  are the river width and runoff height, respectively.

294 In the general phase (Figure 3b), we assume that the water flow represents uniform flow in  
 295 open channels. According to the law of energy conservation, the actual liquid element flow  
 296 energy equation of rivers in grids should be as follows:

$$297 \quad z_1 + \frac{p_1}{\rho g} + \frac{v_1^2}{2g} = z_2 + \frac{p_2}{\rho g} + \frac{v_2^2}{2g} + h_w \quad (3)$$

298 where  $z_1$  and  $z_2$  are the position heads of the inlet and outlet, respectively (m);  $p_1$  and  $p_2$   
 299 are the air pressures at the inlet and outlet, respectively ( $\text{kN m}^{-2}$ );  $\rho = 1000$  is the density of  
 300 water ( $\text{kg m}^{-3}$ );  $g = 9.81$  is the gravitational constant ( $\text{m s}^{-2}$ );  $v_1$  and  $v_2$  are the initial and end  
 301 velocities, respectively ( $\text{m s}^{-1}$ ); and  $h_w$  is the total head loss (m). The total head loss can be  
 302 divided into the frictional head loss ( $h_f$ ) and local head loss ( $h_j$ ) as follows:

$$303 \quad h_w = \sum h_f + \sum h_j \quad (4)$$

$$304 \quad h_f = \sum \lambda \frac{L_R}{4R} \frac{v^2}{2g}, \lambda = \frac{24}{Re} \quad (5)$$

$$305 \quad h_j = \sum \zeta \frac{v^2}{2g}, \zeta = \frac{2gL_b}{C^2R} \left( 1 + \frac{3}{4} \sqrt{\frac{b}{r}} \right) \quad (6)$$

$$306 \quad C = \frac{1}{n} R^{1/6} \quad (7)$$

$$307 \quad n = (n_0 + n_1 + n_2 + n_3 + n_4) \times m_5 \quad (8)$$

308 where  $\lambda$  is the frictional head loss coefficient, which can be calculated using an empirical  
 309 formula including the Reynolds number ( $Re$ );  $R$  is the hydraulic radius (m);  $\zeta$  is the local  
 310 head loss coefficient;  $L_b$ ,  $b$  and  $r$  are the length (m), width (m) and bend radius (degree) of  
 311 the river curve, respectively;  $C$  is the Chezy coefficient ( $m^{1/2} s^{-1}$ ); and  $n$  is the channel  
 312 roughness, which can be calculated using Eq. 8. In Eq. 8,  $n_0$  to  $n_4$  represent the basic  
 313 roughness of natural channels, the influence of irregular water surfaces, the influence of  
 314 changes in the channel cross section shape and size, the influence of water-blocking substances  
 315 and the influence of plants, respectively; and  $m_5$  is the river-winding coefficient, which is  
 316 equal to 1 in our research.

317 Since the river bend degree is not similar to the other variables, it is difficult to unify  
 318 the variables related to river bends, so we proposed the concept of the 1-km bend radius  
 319 equivalent and converted the length sum of each river bend to the same magnitude to unify the  
 320 river bend degree in the analyzed basin. Therefore, the total bending length of 1km bending  
 321 radius equivalent  $L'_b$  in the grid can be expressed by the bending radius  $R_b$  and bending  
 322 angle  $r$  of each bend:

$$323 \quad L'_b = \sum \frac{r}{360^\circ} \times 2\pi \times \frac{R_b}{1km} \quad (9)$$

324 To more realistically reflect the characteristics of grassland rivers, we set the overflow  
 325 coefficient to determine whether overflow occurs when a flood peak passes according to the  
 326 real-time river depth. When a flood phase occurs (Figure 3b), the raster channel is reset to a  
 327 state with no bend and a base river length. After the flood passes (as represented by the recovery  
 328 phase in Figure 3b), the river gradually begins to bend with the influence of the geostrophic  
 329 deflection force and other factors; that is, the river length gradually recovers to the actual river  
 330 length, and curved reaches reappear. The river length, curve length and bending angle of the  
 331 three periods can be expressed as:

$$332 \quad f(L_R, L'_b, r) = \begin{cases} \text{Max}(L_R, L'_b, r), & \text{General phase} \\ \text{Min}(L_R, L'_b, r), & \text{Flood phase} \\ t_m/t_n \text{Max}(L_R, L'_b, r), & \text{Recovery phase} \end{cases} \quad (10)$$

333 where,  $t_m$  and  $t_n$  are respectively the time from the last overflow to the present and the total  
 334 time it took for the river to recover to bend.

335

### 336 2.2.2.3 FLC module operation and output unit

337 The operation and output unit summarizes the parameters calculated by the first two  
 338 units at each moment, calculates the time and amount of flowing water moving to the next grid  
 339 cell, and iteratively describes the flow situation of each section of the basin in the whole  
 340 simulation period layer by layer. First, through the flow direction, we can calculate the number

341 of grid layers  $j$  needed for each grid point to flow to the drainage outlet of the basin. If the  
 342 row and column numbers of the watershed grid points are set as  $m$  and  $n$ , respectively, then  
 343 the grid point layer being processed can be expressed as  $m(j)$  and  $n(j)$ , respectively. The  
 344 flow in a given grid cell at moment  $t$  can be expressed as  $Q(t)_{m(j),n(j)}$ , and the time ( $\Delta t$ ) of  
 345 the runoff flow to the next grid point at this moment can be calculated as follows:

$$346 \quad \Delta t = \frac{L_R}{\bar{v}} = \frac{L_R}{0.5 \times (v_1 + v_2)} \quad (11)$$

347 where  $L_R$  is the river length and  $\bar{v}$  is the average discharge velocity. Since our unit time is 3  
 348 hours, when the runoff time is not an integer, we divide the flow according to the integer time  
 349 so that the flow out of the grid at time  $t$  is  $q(t)_{m(j),n(j)}$ :

$$350 \quad q(t + fix(\Delta t))_{m(j),n(j)} = Q(t)_{m(j),n(j)} \times \frac{fix(\Delta t)}{\Delta t} + Q(t - 1)_{m(j),n(j)} \times$$

$$351 \quad \frac{\Delta(t-1) - fix(\Delta(t-1))}{\Delta(t-1)} \quad (12)$$

352 where  $fix$  is a downward rounding function.

353 The above equations represent the case in which upstream grid inflow is not considered.  
 354 When upstream grid inflow is present, we first calculate the initial flow obtained by the grid  
 355 cell as follows:

$$356 \quad Q(t)_{m(j),n(j)} = Qsim(t)_{m(j),n(j)} + \sum_1^{dir} q(t)_{m(j+1),n(j+1)} \quad (13)$$

357 where  $Qsim(t)$  is the flow rate in each grid cell calculated by the flow generation module and  
 358  $dir = 1$  to  $7$  represents 1 to 7 upstream convergence directions. Notably, a given grid cell has  
 359 a total of eight possible directions: north, northeast, east, southeast, south, southwest, west, and  
 360 northwest. In the confluence process, if the water flowing from all eight directions flows into  
 361 the central point, we regard this grid cell as a depression. When the water surface exceeds the  
 362 lowest surrounding elevation within the grid, it is discharged in this direction; please refer to  
 363 section 2.2.2.1 for details.

364

## 365 2.3 Validation

### 366 2.3.1 Verification system

367 To verify the accuracy and applicability of the MYEH model, we adopted dual-drive  
 368 data source adaptation, traditional model comparison and measured data inspection methods.  
 369 The dual-drive data source adaptation used in this study refers to the drive data generated under  
 370 two different observation systems, the China Meteorological Driven Data Set (CMFD) and  
 371 Global Land Data Assimilation System Noah Land Surface Model L4 (GLDAS-Noah); these  
 372 datasets are brought into the MYEH model to calculate and simulate the ecohydrological  
 373 process of the XRB. The comparison with the traditional model is mainly reflected in the  
 374 confluence model calculation, in which the length of each grid cell is fixed and the head loss  
 375 of the river is not included. The measured data test includes a comparison and verification of  
 376 the daily discharge data collected at the Chinese National Hydrological Station in the basin,

377 the discharge data recorded at the self-built automatic detection hydrological stations at three  
 378 river sections and the artificially measured real-time discharge data obtained through value  
 379 simulations (Figure 2b).

380

### 381 2.3.2 Multiobjective calibration

382 To evaluate the MYEH model simulations in the studied semiarid grassland more  
 383 comprehensively, this paper selects several evaluation indexes. We used the coefficient of  
 384 determination ( $R^2$ ), Nash-Sutcliffe efficiency coefficient (NSE) (Nash & Sutcliffe, 1970), bias  
 385 between the simulated and measured values (Bias), transform root mean square error (TRMSE),  
 386 mean absolute error (MAE), and Kling-Gupta efficiency (KGE) to quantify the mismatches  
 387 between the simulated and tested data. These metrics can be expressed as follows:

$$388 \quad R^2 = 1 - \frac{\sum_{t=1}^N (Q_{s,t} - \bar{Q}_{o,t})^2}{\sum_{t=1}^N (Q_{o,t} - \bar{Q}_{o,t})^2} \quad (14)$$

389 where  $Q_{s,t}$  and  $Q_{o,t}$  are the simulated and observed runoff, respectively, at time  $t$  and  $\bar{Q}_{o,t}$   
 390 is the mean of the observed and predicted data over the calibration period.

391 *NSE* compares the predicted values to the 1:1 line between the measured and predicted  
 392 values rather than the best regression line through the points. *NSE* values range from 1 (optimal)  
 393 to  $-\infty$ , and this metric been frequently used as a hydrologic model calibration objective:

$$394 \quad NSE = 1 - \frac{\sum_{t=1}^N (Q_{o,t} - Q_{s,t})^2}{\sum_{t=1}^N (Q_{o,t} - \bar{Q}_{o,t})^2} \quad (15)$$

$$395 \quad Bias = \frac{1}{N} \sum_{t=1}^N \bar{Q}_{s,t} - E(Q_{o,t}) \quad (16)$$

396 where  $E(Q_{o,t})$  is the expected observed value.

397 Following prior studies (Misirli et al., 2003; Tang et al., 2007), one of the objectives  
 398 analyzed herein emphasizes low flow errors using the Box-Cox (Box & Cox, 1964) TRMSE,  
 399 as shown in equation (12):

$$400 \quad TRMSE = \sqrt{\frac{1}{N} \sum_{t=1}^N (\hat{Q}_{s,t} - \hat{Q}_{o,t})^2}, \text{ where } \hat{Q} = \frac{(1+Q)^\lambda - 1}{\lambda} \quad (17)$$

401 where  $\hat{Q}_{s,t}$  is the Box-Cox-transformed simulated runoff at time  $t$  and  $\hat{Q}_{o,t}$  is the Box-Cox-  
 402 transformed observed runoff at time step  $t$ . The summation is performed from time step 1  
 403 through the number of time steps in the calibration period ( $N$ ).  $\hat{Q}$  represents the Box-Cox-  
 404 transformed runoff value  $Q$ , where  $\lambda = 0.3$ . The Box-Cox transformation, in addition to  
 405 emphasizing low flow periods, also serves to reduce the impacts of heteroscedasticity in the  
 406 RMSE calculation.

$$407 \quad MAE = \frac{1}{N} \sum_{t=1}^N |Q_{o,t} - Q_{s,t}| \quad (18)$$

408 The KGE (Eq. 17) (Gupta et al., 2009; Knoben et al., 2019) is based on the decomposition  
 409 of NSE into its constitutive components (correlation, variability bias and mean bias), addresses  
 410 several perceived shortcomings in NSE (although there are still opportunities to improve the  
 411 KGE metric and to explore alternative ways to quantify model performances) and is  
 412 increasingly used for model calibrations and evaluations:

$$413 \quad KGE = \sqrt{(1 - \gamma)^2 + (1 - \alpha)^2 + (1 - \beta)^2} \quad (19)$$

414 where  $\gamma$ ,  $\alpha$ , and  $\beta$  are the linear correlation coefficients, the ratio of their standard deviations  
 415 and the ratio of the mean values of the simulated and measured values, respectively.  
 416 Additionally,  $P$  values were used to test the sample variance in the measured and simulated  
 417 values, and the significance level was set to 0.01. When the  $p$  value was less than 0.001, there  
 418 was a highly significant difference.

419

## 420 2.4 Overflow frequency analysis

421 To further understand the steppe river overflow phenomenon, the frequency and  
 422 locations of overflow events and the vegetation status of the basin during the whole study  
 423 period are assessed. We use a cross-wavelet analysis to study the periodic interactions between  
 424 monthly overflow times and precipitation, the leaf area index (LAI) to reflect the vegetation  
 425 status, and the southern oscillation index (SOI) and sea surface temperature (SST) to reflect  
 426 climate change in the NINO3.4 region. The Morlet wavelet is selected as the wavelet type, and  
 427 the confidence level is set to 95%. For detailed introductions of the wavelet transform, see Sang  
 428 (2013) and Nourani et al. (2014).

429

## 430 3 Data

431 The data used in this paper can be divided into product data and measured data, which  
 432 mainly include meteorological data, remote sensing data and verification data. The spatial  
 433 resolution and time span of these data are shown in Table 3.

434 The meteorologically driven data include CMFD and GLDS-NOAH data, among which  
 435 CMFD mainly includes 2-m temperature (T), precipitation (P), relative humidity, 10-m wind  
 436 speed, longwave and shortwave radiation and air pressure data (Yang et al., 2010). Since the  
 437 temporal coverage of the CMFD does not include 2019 or 2020, the meteorologically driven  
 438 data representing these two years are obtained by spatial interpolation using data from the self-  
 439 built stations. The GLDAS-NOAH data are obtained from NASA's Global Land Data  
 440 Assimilation System (Beaudoin & Rodell, 2020; Rodell et al., 2004). To match the simulation  
 441 time, we used GLDAS-2.0 data from 1980 to 2000 and GLDAS-2.1 data from 2001 to 2020.  
 442 For the remote sensing data, Leaflet through the open-source JavaScript library and high-  
 443 resolution Google historical satellite images downloaded for interactive mapping were used.  
 444 The image tile level was 17, and the spatial resolution was 2.15 m. The verification data  
 445 included data recorded at China's national stations, self-built hydrological weather stations and  
 446 measured artificial river flow data (see Figure 2b and Table 1 for the specific location and

447 information of each station). The vegetation data were obtained using Global Land Surface  
448 Satellite (GLASS) product data statistics (Liang et al., 2013a; Liang et al., 2013b); this product  
449 is spatially and temporally continuous, without gaps or missing values, and the wideband  
450 longwave emissivity product is the first product in the world with an 8-day temporal resolution  
451 and 1-km spatial resolution (Liang et al., 2020). The SOI and SST data were provided by the  
452 official website of the Bureau of Meteorology of the Commonwealth of Australia 2021 and  
453 Weatherzone based on data from the Bureau of Meteorology.

454

455 **Table 3.** Characteristics of the two meteorological datasets.

456

## 457 **4 Results and discussion**

### 458 4.1 Simulation validation of the MYEH runoff generation and confluence processes

459 The meteorologically driven data contained in the CMFD and GLDAS-NOAH datasets  
460 were introduced into the MYEH model to simulate the runoff generation and confluence  
461 processes in the XRB from 1980 to 2020, and the river discharge simulated by the model was  
462 verified using the station data shown in Figure 2b. The results are shown in Figure 4 and Table  
463 4.

464 Figure 4b is a Q-Q plot analysis showing the daily river discharge measured at the XRB  
465 National Hydrographic Station section. According to the kurtosis and skewness of the daily  
466 discharge data, it is not difficult to see that the XRB river discharge presents skewed  
467 distribution characteristics, indicating that the discharge at this section is far below the mean  
468 value. The daily discharge measurements below the mean value are much higher than the  
469 expected value of  $0.554 \text{ m}^3 \text{ s}^{-1}$ , indicating that slow surface runoff is normal in the XRB and  
470 reflecting the characteristics of a trickling grassland river in a nonflood period (Coe et al., 2011;  
471 Metivier et al., 2016).

472 The MYEH model performs well when simulating river runoff using two kinds of  
473 meteorologically driven data. From the perspective of evaluation indexes, the  $R^2$  and NSE  
474 values were both greater than 0.9, and the KGE value was less than 0.3, indicating that the  
475 MYEH model performed well when controlling the trend of the overall ecohydrological  
476 process (Figure 4a). The daily discharge simulation results obtained using the two  
477 meteorological driven datasets show that the discharge simulated using CMFD was slightly  
478 better than that simulated using the GLDAS-NOAH dataset in the daily flood peak simulations;  
479 specifically, some deviation occurred in the maximum daily flood peak outputs within the year.  
480 The test results of the three automatic hydrological stations show that the simulated results  
481 were relatively accurate (Figure 4c-e), and the corresponding  $R^2$  and NSE values were slightly  
482 lower than the test results obtained at the national hydrological station section. The manual  
483 flow measurement results show that the NSE value of the simulated and observed flow values  
484 is high, while the corresponding  $R^2$  value is low. The distribution of the scatter diagram is  
485 relatively convergent, and the linear fitting and 1:1 line are also relatively consistent, indicating  
486 that the overall results are reliable and the process simulation error is small.

487

488 **Figure 4.** (a) Comparison of the simulated and measured daily sectional discharge at a national  
489 hydrological station obtained using two meteorologically driven datasets with the MYEH  
490 model; (b) Q-Q plot of daily discharge in the XRB; (c-e) comparison of the simulated and  
491 measured daily sectional discharge at three automatic hydrological stations using two  
492 meteorologically driven datasets with the MYEH model; (f) comparison of the simulated and  
493 measured daily sectional discharge at seven measuring sites using the CMFD; and (g)  
494 comparison of the simulated and measured daily sectional discharge at seven measuring sites  
495 using the GLDAS-NOAH dataset. The green points in (a) to (e) are the values observed at the  
496 national hydrological station.

497

498 **Table 4.** Six evaluation value of simulated runoff in XRB using two data sources.

499

500 The results show that the MYEH model combined with the evapotranspiration and  
501 runoff generation and confluence modules can effectively simulate the runoff process of each  
502 grid section representing the grassland river channel. Combined with the river location of the  
503 three inspection sections, the downstream flow simulations conducted in the basin are also  
504 better than those in the upstream flow-producing area; this result can be mainly summarized as  
505 the influence of different flow-producing methods and measurement accuracy insufficiencies.  
506 The runoff generation modes of steppe rivers can be mainly divided into two types: runoff  
507 generation on the mountain slopes and groundwater outcropping in front of mountains (da Silva  
508 et al., 2018; Gupta et al., 2019). Most of the runoff generation models in the basin conform to  
509 the Sim precipitation and soil water storage module (Zhang et al., 2021), and only a few grid  
510 points contain outcropping groundwater (although such areas can also be simulated using the  
511 soil water storage principle) (Liang et al., 2012; Wagener et al., 2004); however, some  
512 deviations exist (Li et al., 2015; Lopes & Canfield, 2004). On the other hand, the grassland  
513 river characteristics in the upstream flow-producing areas mostly represent wetlands  
514 (floodplains) with soil water contents close to or at saturation (Tang et al., 2020; Wang et al.,  
515 2014). In the actual flow measurements collected in such areas, although we selected river  
516 sections in wetlands (floodplains) that met the flow measurement standards, the verification  
517 data did not contain mid-soil flow information, further leading to verification errors (Bendjoudi  
518 et al., 2002; Wagener et al., 2004).

519 Compared with the validation results of the data recorded at the two hydrological  
520 stations, the tested accuracy of the manual flow measurements was the lowest; this result can  
521 be summarized with two reasons. Firstly, due to the rich data of hydrology station and  
522 automatic flow measurements, the model will be inclined to the site with rich data when scaling  
523 parameters, while there are only a few measured data of manual flow measurement, so the  
524 weight of the data will be reduced and the error will become larger. The other reason is also  
525 related to the characteristics of steppe rivers; during the flood period, sandy riverbeds do not  
526 easily maintain stable shapes (Staudt et al., 2019), and semiarid grasslands experience high

527 wind speeds in both the spring and summer rainy seasons (Li et al., 2021), thus affecting the  
528 river flow measurements.

529

#### 530 4.2 Parameter optimization and sensitivity analysis

531 Model parameters can be defined as quantities that are used to represent the physical or  
532 ecohydrological characteristics of a watershed and remain constant during the simulation  
533 process (Melsen & Guse, 2019; Pfannerstill et al., 2015; Qi et al., 2019). The optimization of  
534 parameters in the MYEH model can make automatic adjustments using a variety of evaluation  
535 indexes to ensure that the simulated and observed runoff values match well (Song et al., 2012).  
536 Figure 5a-c describes model parameter optimization process through the use of three evaluation  
537 indexes (due to a large number of iterations, only partial results are shown in the figure). The  
538 results showed that the related variables of some runoff production modules dominated by soil  
539 water migration still showed convergence trends even under different rating indexes; this  
540 directly reflected the characteristics of the basin among the parameter values (Huang et al.,  
541 2015a; Yokoo & Kazama, 2012).

542 The parameters that control soil, snowmelt and river channels are all important input  
543 variables in ecohydrological models, and subtle changes in these parameters directly affect the  
544 stability of the models. Therefore, it is particularly important to discuss the influence of the  
545 parameters utilized in each module on the practical applications of the model (Guse et al., 2016;  
546 Pfannerstill et al., 2015). The parameters considered in the Sim module and snow routine unit  
547 mainly affect the change in yield over time (Croke & Jakeman, 2004; Huang et al., 2015b), and  
548 the FLC module parameters directly affect runoff collection (Reaney et al., 2014). All three of  
549 these parameter groups alter the flood propagation process to a certain extent. Therefore, the  
550 average simulation results obtained for these two modules and one routine unit were increased  
551 or decreased by 1, 2, 5, 7.5, 10, 12.5, 15, 20, 25, 30% and no change, and a total of 21 conditions  
552 were analyzed, respectively. The results are shown in Figure 5d-f.

553 The parameter sensitivity analysis results are all within the acceptable range. Among  
554 them, changes in the snow routine parameters had the smallest impact on the simulated runoff.  
555 When the change range was greater than 5%, an increase in the snow process parameters had  
556 a greater impact on the simulation accuracy than a decrease in the snow process parameters.  
557 The parameters of the Sim and FLC modules were much more sensitive than those of the snow  
558 routine unit. When the variation range of the parameters of the above two modules exceeded  
559 5%, the simulated  $R^2$  and NSE values dropped to approximately 0.7 and 0.55, respectively  
560 (Figure 5d-e). The KGE index shows that when the variation range exceeded 10, the model  
561 accuracy significantly decreased (Figure 5f).

562

563 **Figure 5.** Parameter optimization (a-c) and parameter sensitivity analysis (d-f) results obtained  
564 for the MYEH model.

565

### 566 4.3 Applicability analysis

567 The applicability analysis conducted in this paper focuses on the universality of  
568 different driving datasets in the XRB. The results show that the runoff simulation results  
569 obtained using two different meteorological driving datasets were basically distributed on the  
570 1:1 line between the  $R^2$  and NSE values, and the TRMSEs of most simulated values were less  
571 than 0.6 (Figure 6). As a test index considering correlation, variability bias and mean bias, the  
572 KGE values remained between 0 and 0.4 on the whole, and the closer the  $R^2$  and NSE values  
573 of the two simulated values were, the better the KGE evaluation result was.

574 In the simulation comparison, the errors resulting from data sources increased when the  
575 lower runoff or base flow were simulated (Balin et al., 2010; Faramarzi et al., 2015; Sikorska  
576 et al., 2015). In addition, collapse phenomena with high  $R^2$  values but poor NSE, KGE and  
577 TRMSE values occurred rarely in both the non-icebound period and the icebound period but  
578 occurred slightly more frequently in the non-icebound period than in the icebound period.  
579 These outliers indicate that although the results conform to the change rule in the whole time  
580 series, there is a certain deviation. The main reason for this phenomenon is that there a certain  
581 difference exists in the precipitation data between the two meteorologically driven datasets  
582 (Renard et al., 2011; Schoups & Nasser, 2021), resulting in consistent flood peak occurrence  
583 times (consistent with the temporal rules) in the runoff generation simulations but deviating  
584 runoff (base flow) flood peak values.

585

586 **Figure 6.** Comparison of the MYEH model-simulated runoff discharge during the nonfreezing  
587 period (a) and base flow during the freezing period (b) in the XRB as determined using the  
588 CMFD and GLDAS-NOAH data sources. In this figure, NSE and  $R^2$  are plotted on the  $X$  and  
589  $Y$  axes, respectively, KGE is plotted in color, and TRMSE is plotted using the size of the  
590 markers. The black arrow points in the direction of decreasing flow or base flow. The red arrow  
591 indicates the tendency of both data-source simulations to collapse. NSE: Nash-Sutcliffe  
592 efficiency; KGE: Kling-Gupta efficiency; and TRMSE: Box-Cox transformed root mean  
593 square error.

594

### 595 4.4 Flood process

596 In view of the good applicability and strong stability of the MYEH model in the XRB,  
597 we further investigated the confluence mode of the FLC module (runoff in this mode is referred  
598 to as  $Q_s$ ) and two common confluence modes (we called the runoff discharge in these two  
599 confluence modes  $Q_{s1}$  and  $Q_{s2}$ ). The confluence model that does not consider the actual river  
600 length, river bend or overflow and the confluence model that considers the actual river length  
601 or river bend but does not consider overflow were compared and analyzed in their simulation  
602 of the four flood modes. First, we selected two 1/20-year frequency floods and two 1/50-year  
603 frequency floods in the simulation period. Two driving datasets and three confluence modes  
604 were used to simulate the flood process at the 3-hour scale. Yellow and red five-pointed stars  
605 were used to indicate the initial times at which overflows started in the tributaries and in both

606 the tributaries and mainstream. The flow data measured at the XRB National Hydrological  
607 Station section are shown in [Figure 7](#).

608 The results show that the flood peak times simulated by the two datasets at the diurnal  
609 scale are basically the same, and only the peak flood value differs slightly; this is consistent  
610 with the previous results regarding the universality of the XRB for different driving datasets.  
611 On the whole, Qs1, which does not consider the actual river length, river bend or flood, resulted  
612 in the fastest flood arrival time and the shortest flood duration. Qs2, which considers the actual  
613 river length or river bend, resulted in the latest flood arrival time and the longest flood duration.  
614 Qs, as simulated by FLC, had outputs in the middle of the two results described above ([Figure](#)  
615 [7](#)).

616 Both floods that occurred in 1987 were triggered by single heavy rain events. The  
617 rainfall event that occurred on August 11<sup>th</sup> was short but intense, while the rainfall event that  
618 occurred on August 26<sup>th</sup> was light but prolonged. Accordingly, on August 11<sup>th</sup>, runoff reached  
619 the flood peak within 3 to 6 hours, while the runoff peak measured on August 26<sup>th</sup> was not as  
620 urgent as the former ([Figure 7a](#)). In 1998, many basins in China experienced extensive regional  
621 floods, and precipitation in the XRB was abundant. The year 1998 mainly included four floods  
622 caused by continuous precipitation, among which two floods showed a bimodal pattern due to  
623 short interruptions in precipitation ([Figure 7b](#)). In 2004 and 2012, extremely rare heavy rains  
624 occurred and caused extreme flood events. The runoff simulation results of different confluence  
625 modes also showed similar differences in these years. The flood peak of the Qs1 mode was 3  
626 to 6 hours earlier than that of the FLC mode, while the flood peak of the Qs2 mode was 3 to 6  
627 hours later than that of the FLC mode. The flood waveform and numerical runoff characteristics  
628 simulated by the three modes were basically consistent. In particular, when river overflows  
629 occurred, the flood peak value simulated by the FLC mode was slightly higher than that  
630 simulated by the Qs1 mode ([Figure 7c, d](#)).

631  
632 **Figure 7.** Simulations of the 3-hour flood process under three confluence modes using the  
633 CMFD and GLDAS-NOAH data sources. Figures 7(a) to 7(d) show monsoon floods in 1987,  
634 1998, 2004 and 2012, respectively. Qs indicates the MYEH model confluence mode (FLC).  
635 Qs1 indicates the confluence mode in which the actual river length, river bending and overflow  
636 are not considered. Qs2 indicates the confluence mode in which the actual river length and  
637 river bending are considered but overflow is not considered. The orange and red stars represent  
638 the overflow of tributaries and the overflow of main streams and tributaries in a flood event,  
639 respectively.

640  
641 Different confluence modes cause different flood arrival times, flood peak values and  
642 even flood waveforms ([Gao et al., 2004; Wagener & Montanari, 2011](#)). Through a comparison  
643 of the three confluence modes, it can be seen that considering the actual river length and river  
644 bend can result in more realistic simulations of steppe river network characteristics. However,  
645 if the overflow situation is not considered, the arrival time of the flood lags behind, and this  
646 situation is more obvious when the flood peak is larger. As a prominent feature of steppe rivers,  
647 channel overflow events not only advance the arrival times of flood peaks but also increase the

648 flood peak values to a certain extent. To refine and decompose the impacts of overflow events,  
649 we divided the overflows into tributary overflows and mainstream overflows. Since the  
650 mainstream is wider and deeper than the tributaries, we found that overflows first occur in  
651 tributaries during the whole simulation period and then occur in the mainstream when the flood  
652 becomes sufficiently large.

653 First, we take 1987 and 1998 as examples to study the influence of tributary overflows  
654 on the confluence of steppe rivers. The two minor floods that occurred on August 7<sup>th</sup>, 1987,  
655 and June 2<sup>nd</sup>, 1998, showed that the difference between Qs and Qs1 was mainly that the  
656 overflow event occurred slightly earlier in Qs1 than in Qs; the two overflow values were  
657 basically consistent. When tributary overflow occurred, the Qs-derived peak value basically  
658 exceeded the Qs1-derived value, mainly reflecting the influence of river overflow on the runoff  
659 flood peak (Figure 7a, b). In the extreme flood events of 2004 and 2012, when overflows  
660 occurred in both the tributaries and mainstreams, not only did the Qs-derived peak exceed the  
661 Qs1-derived peak, but the slope of the simulated runoff also gradually increased, and the arrival  
662 time of the flood peak continually approached the Qs1-derived linear confluence value,  
663 reflecting the influence of river overflows on the arrival time and value of the flood peak  
664 (Figure 7c, d). In terms of the overflow process, the length of the flow path was shortened and  
665 the flow velocity was reduced by river bends, thus enabling the flow to converge more quickly  
666 to the downstream section (Cervantes et al., 2020; Knighton et al., 2014). A shorter river  
667 distance serves to reduce losses associated with evaporation, infiltration and other processes  
668 and improves the flood peak value compared with that derived using the mode that does not  
669 consider overflow (Krasnostein & Oldham, 2004).

670

#### 671 4.5 Response analysis of overflow frequency to climate and ecology

672 Simply speaking, the overflow of river channels is a special situation in which an  
673 abundant inflow of water from the upstream region leads the river to overflow, thus disturbing  
674 the channel parameters and influencing the confluence of river networks. From the perspective  
675 of the hydrological function of a basin, river overflows are extremely destructive, as they lead  
676 not only to frequent riverbank collapses and diversions but also easily lead to extreme  
677 hydrological events such as decreased storage capacities, a steeply rising floods, and increased  
678 river sediment loads. In addition, from the perspective of vegetation ecology, river overflows  
679 can also lead to swamp conditions in valley wetlands and community succession in ecosystems  
680 dominated by plants and microorganisms through the resulting changes in soil moisture, ion  
681 concentrations and nutrient availabilities. Although it is difficult to directly define or judge the  
682 advantages and disadvantages of these succession processes, these processes represent another  
683 scientific question we hope to explore with the help of the proposed grassland watershed  
684 ecohydrological model.

685 River overflows are not only directly related to precipitation but are also related to the  
686 regional vegetation and river stability. First, according to our simulation of the ecohydrological  
687 process in the XRB, we created a diagram of the annual average overflow frequency in the  
688 study area and the correlation distribution between overflows and the regional vegetation status  
689 (Figure 8a). The overflow frequency results showed that the average annual overflow

690 frequency was more than once a year in the upper reaches of the analyzed basin, especially in  
691 the river channel in the northeastern part of the study area and in the Hilltara wetland in the  
692 central and eastern parts of the study area, as the river channel in the upper reaches of the river  
693 and the wetland were relatively shallow and prone to overflowing (Bornette & Amoros, 1991).  
694 The northwestern part of the study area contains the Xilinhote Reservoir, which has low terrain  
695 and a large catchment area, so we did not analyze this region.

696 The correlation between overflows and ecological conditions showed that the overflow  
697 frequency in the mainstream (OFN) was strongly correlated with the vegetation conditions, and  
698 the correlation between LAI and the mainstream grid prone to overflowing exceeded 0.5. The  
699 correlations between OFN and the vegetation status in tributaries and nonmainstream streams  
700 were higher in the south and lower in the north. According to the precipitation trend analysis,  
701 from 1980 to 2020, LAI and OFN as well as precipitation ( $17.18 \text{ mm } 10\text{a}^{-1}$ ) and OFN ( $0.84$   
702  $10\text{a}^{-1}$ ) showed obvious increasing trends (Figure 8b), while LAI, which represents the  
703 vegetation conditions, showed a slight decreasing trend ( $-0.04 \text{ } 10\text{a}^{-1}$ ). Moderate overflow will  
704 improve the ecology of wetland vegetation in the valley. For example, snowmelt and ice-melt  
705 runoff in spring will increase the soil moisture content of wetland in the valley after overflow,  
706 making it easier for the wetland to turn green. It is believed that the real cause of wetland  
707 vegetation degradation in XRB valley should be the combination of riparian vegetation  
708 degradation and stunting caused by overgrazing. These results were consistent with the  
709 conclusion that the increase in OFN was related to the increase in precipitation and the  
710 degradation of vegetation analyzed in the previous section; further, these results are also  
711 consistent with the conclusion reached by Xu et al. (2009) in their study on the effect of the  
712 riparian vegetation ecological status on overflow events in the lower reaches of the Tarim River,  
713 another arid region.

714 To further study the response trend of OFN to the environmental changes that have  
715 occurred in the last 41 years, we conducted periodic analyses of OFN with precipitation,  
716 vegetation, SOI, and SST in the NINO3.4 region using cross-spectrum analysis techniques.  
717 The significant cross-wavelet energy results obtained between OFN and precipitation, LAI,  
718 SOI and SST were mainly distributed in periods from 5 to 7 years and from 10 to 13 years  
719 (Figure 8c-f), among which the 10-13-year period was the most significant, indicating that  
720 overflows in the XRB have a strong corresponding relationship with global climate change,  
721 such as El Niño changes, and that these two processes are closely related (He et al., 2015;  
722 Kundzewicz et al., 2010; Minville et al., 2010).

723 In addition, in some years, precipitation and LAI also had significant and strong  
724 interactions with OFN in periods ranging from 1 to 4 years and from 2 to 4 years, respectively,  
725 further indicating that overflow events strongly interacted with precipitation and LAI with short  
726 periods. In the strong interaction cycle lasting 10 to 13 years, the interactions between OFN  
727 and precipitation and between OFN and LAI were in the positive phase; that is, no lag effect  
728 was observed between the overflows and local meteorological or vegetation conditions. The  
729 phase difference between OFN and SST was approximately  $30^\circ$ , indicating that overflow  
730 events in the XRB have a lag period of approximately 2 years in response to global climate  
731 change.

732 Overall, the MYEH model that considers river overflow events helps us to understand  
733 that the special steppe river overflow phenomenon is closely related to the local precipitation,  
734 vegetation status, global climate change and other factors; further, this model helps reveal the  
735 unique ecohydrological processes and response mechanisms of typical steppe ecosystems.

736

737 **Figure 8.** (a) Average annual overflow frequency and the correlation between overflows and  
738 vegetation status. (b) Trend analyses of precipitation, LAI, and OFN from 1980 to 2020. (c-f)  
739 The cross-wavelet energy spectrum analyses of the OFN with precipitation, LAI, SOI and  
740 NINO3.4 SST. The 5% significance level against red noise is shown as a thick contour line.  
741 The relative phase relationships are shown as arrows (with in-phase relationships pointing right  
742 and anti-phase relationships pointing left).

743

#### 744 4.6 Existing problems and uncertainty analysis

##### 745 4.6.1 Refine the overflow process

746 Although we optimized the grassland river confluence process by setting the overflow  
747 coefficient and other methods, we still found that the simulated flow value at the maximum  
748 flood peak time was slightly higher, while the flood peak was slightly lower at the later time  
749 units ([Figure 4](#)); these results indicated that our confluence speed simulation results were still  
750 overestimated to some extent. A further subdivision of the overflow process (type) may be  
751 helpful for obtaining a more detailed optimization. First, do overflow events permanently reset  
752 channels? This question corresponds to the dynamic treatment of the recovery period following  
753 diffuse flow conditions. The second step is to distinguish overflow events into temporary and  
754 dam break overflow. These errors tend to focus on the flow increases caused by the  
755 summertime rainy season and the spring flood caused by springtime snowmelt. Small  
756 overestimations can be seen in both utilized datasets ([Figures 4 and 7](#)). In a more refined river  
757 channel description, it is critical to optimize the confluence process in the future to determine  
758 whether the overflow coefficients can be graded and the sensitivity of the analyzed reach can  
759 be graded, aiming to realize dynamic overflow simulations inside the river network grid cells  
760 for flood control in small grassland river basins. In addition, overflow will affect soil moisture  
761 and vegetation, so the ecological process simulation of a watershed, especially the simulation  
762 of wetland ecological process after overflow, is also the direction for further optimization and  
763 improvement.

764

##### 765 4.6.2 Optimize the parameter selection system

766 The MYEH model constructed in this study adopts the overall parameter adjustment  
767 principle and comprehensively judges the results using multiple evaluation indexes to select  
768 the simulation results with the highest accuracies, smallest errors and most physically  
769 significant parameter combinations as effectively as possible. Such an evaluation system is  
770 considered comprehensive but still has room for improvement. For example, a variety of  
771 verification methods that aim to ensure data accuracy are included in the evaluation system;

772 the evapotranspiration and production confluence module parameters are adjusted  
773 simultaneously; and the simulation results are evaluated. In addition, simulation process  
774 parameters such as the soil moisture content could also be included in the evaluation system to  
775 improve the ecohydrological process simulation accuracy.

776

#### 777 4.6.3 Subsequent module design

778 Through multiple ecological-hydrological process simulations, we found that a certain  
779 error still exists when simulating the water balance in grassland wetlands. On the one hand,  
780 due to the lack of frozen soil simulations, the water resulting from springtime snowmelt in the  
781 flood season cannot undergo large-scale penetration or flow into the soil, thus leading to  
782 evapotranspiration underestimations; on the other hand, due to this omission, groundwater  
783 recharge is not considered. For the subsequent expansion of the MYEH model, we plan to take  
784 two steps: one step involves improving the FLC module and building frozen soil and  
785 groundwater modules by summarizing and combining existing problems; and the other step  
786 involves considering more ecological-hydrological processes and building modules to  
787 represent the nutrient element cycle, plant growth, grazing disturbances and so on.

788

## 789 5 Conclusion

790 Aiming to represent runoff in a semiarid steppe basin with variable meandering rivers  
791 and steep flood flows, we simulated the 3-hour runoff process in the XRB from 1980 to 2020  
792 by constructing runoff generation and convergence modules in the MYEH model to consider  
793 the dynamic actual river length, river bend and overflow characteristics and discussed the  
794 occurrence frequency and influencing factors of steppe river overflow events. The results show  
795 that the MYEH model has a high accuracy and stability when simulating the ecohydrological  
796 process and can also simulate changes in river overflows, flood peaks and arrival times caused  
797 by the passage of large flood events. With the use of an appropriate eco-hydrological model, it  
798 is helpful to further reveal the special phenomenon of the overflow of steppe rivers. Vegetation  
799 degradation caused by overgrazing and the increase of precipitation in the basin are the main  
800 reasons for the increase of the overflow number of XRB, and there is a two-year lag between  
801 the overflow number and global climate change factors.

802

803 **Acknowledgments:** This research was funded by the National Natural Science Foundation of  
804 China (Nos. 51939006, 51620105003 and 51909122), the Inner Mongolia Major Science and  
805 Technology Projects (Grant Nos. 2020ZD0009 and 2019ZD007), the Inner Mongolia Science  
806 and Technology Plan Project (Nos. 2020 and 2021GG0071), the Ministry of Education  
807 Innovative Research Team (No. IRT\_17R60), the Innovation Team in Priority Areas  
808 Accredited by the Ministry of Science and Technology (No. 2015RA4013), the Inner Mongolia  
809 Industrial Innovative Research Team (No. 2012), and the Research and Innovation Funding  
810 Project for Graduate Students (BZ2020069). We are grateful to the principal investigators and  
811 the teams behind all the datasets used in this study. The CMFD datasets are available at  
812 <http://data.tpdc.ac.cn/en/data/8028b944-daaa-4511-8769-965612652c49/>. The GLDAS Noah

813 datasets are available at <https://ldas.gsfc.nasa.gov/gldas/>. Thanks for Leaflet, the leading open-  
 814 source JavaScript library for mobile-friendly interactive maps, which is available at  
 815 <https://leafletjs.com/index.html>. SOI dataset are available at  
 816 <http://www.bom.gov.au/climate/enso/soi/>. SST dataset are available at  
 817 [https://www.weatherzone.com.au/climate/indicator\\_enso.jsp?c=nino34&p=monthly](https://www.weatherzone.com.au/climate/indicator_enso.jsp?c=nino34&p=monthly). All  
 818 generated methods used in this study can be downloaded from  
 819 [https://github.com/myli1993/MYEH\\_model\\_ver1.0](https://github.com/myli1993/MYEH_model_ver1.0). And generated data can be downloaded  
 820 from <https://zenodo.org/record/5578630#.YW7PgRy-uHs>. The authors declare no conflict of  
 821 interest.

822

823 **Author Contributions:** M.L. developed the initial and final versions of this manuscript and  
 824 analyzed the data. T.L., L.M., L.D., Q.W., Y.W., G.W., H.L., and V.S. contributed their  
 825 expertise and insights to oversee the analysis. S.W. and J.L. helped complete the partial data  
 826 preprocessing.

827

## 828 References

- 829 Al-Humoud, J. M., & Esen, II. (2006). Approximate methods for the estimation of Muskingum flood routing  
 830 parameters. *Water Resources Management*, 20(6), 979-990. doi: 10.1007/s11269-006-9018-2
- 831 Asdak, C., Jarvis, P. G., van Gardingen, P., & Fraser, A. (1998). Rainfall interception loss in unlogged and logged  
 832 forest areas of Central Kalimantan, Indonesia. *Journal of Hydrology*, 206(3), 237-244. doi:  
 833 10.1016/S0022-1694(98)00108-5
- 834 Balin, D., Lee, H., & Rode, M. (2010). Is point uncertain rainfall likely to have a great impact on distributed  
 835 complex hydrological modeling? *Water Resources Research*, 46. doi: 10.1029/2009wr007848
- 836 Beaudoin, H., & Rodell, M. (2020). GLDAS Noah Land Surface Model L4 3 hourly 0.25 x 0.25 degree V2.1.  
 837 *Greenbelt, Maryland, USA, Goddard Earth Sciences Data and Information Services Center (GES DISC)*,  
 838 Accessed: [2021-7-31]. doi: 10.5067/E7TYRXPJKWOQ
- 839 Bendjoudi, H., Weng, P., Guerin, R., & Pastre, J. F. (2002). Riparian wetlands of the middle reach of the Seine  
 840 river (France): historical development, investigation and present hydrologic functioning. A case study.  
 841 *Journal of Hydrology*, 263(1-4), 131-155. doi: 10.1016/s0022-1694(02)00056-2
- 842 BERGSTRÖM, S. (1975). THE DEVELOPMENT OF A SNOW ROUTINE FOR THE HBV-2 MODEL.  
 843 *Hydrology Research*, 6(2), 73-92. doi: 10.2166/nh.1975.0006
- 844 Betson, R. P. (1964). What is watershed runoff? *Journal of Geophysical Research (1896-1977)*, 69(8), 1541-1552.  
 845 doi: 10.1029/JZ069i008p01541
- 846 Birkhead, A. L., & James, C. S. (2002). Muskingum river routing with dynamic bank storage. *Journal of*  
 847 *Hydrology*, 264(1-4), 113-132. doi: 10.1016/s0022-1694(02)00068-9
- 848 Bornette, G., & Amoros, C. (1991). Aquatic vegetation and hydrology of a braided river floodplain. *Journal of*  
 849 *Vegetation Science*, 2(4), 497-512. doi: 10.2307/3236032
- 850 Box, G. E., & Cox, D. R. (1964). An analysis of transformations. *Journal of the Royal Statistical Society: Series*  
 851 *B (Methodological)*, 26(2), 211-243. doi: 10.1111/j.2517-6161.1964.tb00553.x
- 852 Bozorg-Haddad, O., Abdi-Dehkordi, M., Hamed, F., Pazoki, M., & Loaiciga, H. A. (2019). Generalized Storage  
 853 Equations for Flood Routing with Nonlinear Muskingum Models. *Water Resources Management*, 33(8),  
 854 2677-2691. doi: 10.1007/s11269-019-02247-2

- 855 Bozorg-Haddad, O., Hamed, F., Orouji, H., Pazoki, M., & Loaiciga, H. A. (2015). A Re-Parameterized and  
856 Improved Nonlinear Muskingum Model for Flood Routing. *Water Resources Management*, 29(9), 3419-  
857 3440. doi: 10.1007/s11269-015-1008-9
- 858 Cadle, S. H., Dasch, J. M., & Vande Kopple, R. (1987). Composition of snowmelt and runoff in northern Michigan.  
859 *Environmental science & technology*, 21(3), 295-299. doi: 10.1021/es00157a011
- 860 Carraro, F., Valiani, A., & Caleffi, V. (2018). Efficient analytical implementation of the DOT Riemann solver for  
861 the de Saint Venant-Exner morphodynamic model. *Advances in Water Resources*, 113, 189-201. doi:  
862 10.1016/j.advwatres.2018.01.011
- 863 Cervantes, M. S., Hernando, A., Garcia-Abril, A., Valbuena, R., Saornil, J. V., & Manzanera, J. A. (2020).  
864 Simulation of overflow thresholds in urban basins: Case study in Tuxtla Gutierrez, Mexico. *River*  
865 *Research and Applications*, 36(7), 1307-1320. doi: 10.1002/rra.3642
- 866 Chang, C. M., & Yeh, H. D. (2018). Spectral analysis of temporal non-stationary rainfall-runoff processes. *Journal*  
867 *of Hydrology*, 559, 84-88. doi: 10.1016/j.jhydrol.2018.02.017
- 868 Choudhury, P., Shrivastava, R. K., & Narulkar, S. M. (2002). Flood routing in river networks using equivalent  
869 Muskingum inflow. *Journal of Hydrologic Engineering*, 7(6), 413-419. doi: 10.1061/(asce)1084-  
870 0699(2002)7:6(413)
- 871 Coe, M. T., Latrubesse, E. M., Ferreira, M. E., & Amsler, M. L. (2011). The effects of deforestation and climate  
872 variability on the streamflow of the Araguaia River, Brazil. *Biogeochemistry*, 105(1-3), 119-131. doi:  
873 10.1007/s10533-011-9582-2
- 874 Croke, B. F. W., & Jakeman, A. J. (2004). A catchment moisture deficit module for the IHACRES rainfall-runoff  
875 model. *Environmental Modelling & Software*, 19(1), 1-5. doi: 10.1016/j.envsoft.2003.09.001
- 876 da Silva, R. M., Santos, C. A. G., & dos Santos, J. Y. G. (2018). Evaluation and modeling of runoff and sediment  
877 yield for different land covers under simulated rain in a semiarid region of Brazil. *International Journal*  
878 *of Sediment Research*, 33(2), 117-125. doi: 10.1016/j.ijsrc.2017.04.005
- 879 David, C. H., Famiglietti, J. S., Yang, Z. L., & Eijkhout, V. (2015). Enhanced fixed-size parallel speedup with the  
880 Muskingum method using a trans-boundary approach and a large subbasins approximation. *Water*  
881 *Resources Research*, 51(9), 7547-7571. doi: 10.1002/2014wr016650
- 882 David, C. H., Hobbs, J. M., Turmon, M. J., Emery, C. M., Reager, J. T., & Farniglietti, J. S. (2019). Analytical  
883 Propagation of Runoff Uncertainty Into Discharge Uncertainty Through a Large River Network.  
884 *Geophysical Research Letters*, 46(14), 8102-8113. doi: 10.1029/2019gl083342
- 885 David, J. S., Valente, F., & Gash, J. H. (2005). Evaporation of Intercepted Rainfall. In *Encyclopedia of*  
886 *Hydrological Sciences*.
- 887 den Besten, N., Steele-Dunne, S., de Jeu, R., & van der Zaag, P. (2021). Towards Monitoring Waterlogging with  
888 Remote Sensing for Sustainable Irrigated Agriculture. *Remote Sensing*, 13(15). doi: 10.3390/rs13152929
- 889 Ding, Y., & Wang, S. S. Y. (2005). Identification of Manning's roughness coefficients in channel network using  
890 adjoint analysis. *International Journal of Computational Fluid Dynamics*, 19(1), 3-13. doi:  
891 10.1080/10618560410001710496
- 892 Dunne, T., & Black, R. D. (1970). An Experimental Investigation of Runoff Production in Permeable Soils. *Water*  
893 *Resources Research*, 6(2), 478-490. doi: 10.1029/WR006i002p00478
- 894 Faramarzi, M., Srinivasan, R., Irvani, M., Bladon, K. D., Abbaspour, K. C., Zehnder, A. J. B., & Goss, G. G.  
895 (2015). Setting up a hydrological model of Alberta: Data discrimination analyses prior to calibration.  
896 *Environmental Modelling & Software*, 74, 48-65. doi: 10.1016/j.envsoft.2015.09.006
- 897 Gao, Y. H., Lu, S. H., & Cheng, G. D. (2004). Simulation of rainfall-runoff and watershed convergence process  
898 in the upper reaches of Heihe River Basin, July 2002. *Science in China Series D-Earth Sciences*, 47, 1-

- 899 8. doi: 10.1360/04zd0001
- 900 Geng, X. J., Zhou, X. C., Yin, G. D., Hao, F. H., Zhang, X., Hao, Z. C., et al. (2020). Extended growing season  
901 reduced river runoff in Luanhe River basin. *Journal of Hydrology*, 582, 9. doi:  
902 10.1016/j.jhydrol.2019.124538
- 903 Gentry, A. H., & Lopez-Parodi, J. (1980). Deforestation and increased flooding of the upper Amazon. *Science*  
904 (*New York, N.Y.*), 210(4476), 1354-1356. doi: 10.1126/science.210.4476.1354
- 905 Gill, M. A. (1978). Flood routing by the Muskingum method. *Journal of Hydrology*, 36(3), 353-363. doi:  
906 10.1016/0022-1694(78)90153-1
- 907 Goenster-Jordan, S., Ingold, M., Jannoura, R., Buerkert, A., & Joergensen, R. G. (2021). Soil microbial properties  
908 of subalpine steppe soils at different grazing intensities in the Chinese Altai Mountains. *Scientific Reports*,  
909 11(1), 8. doi: 10.1038/s41598-021-81120-y
- 910 Gupta, H. V., Kling, H., Yilmaz, K. K., & Martinez, G. F. (2009). Decomposition of the mean squared error and  
911 NSE performance criteria: Implications for improving hydrological modelling. *Journal of Hydrology*,  
912 377(1-2), 80-91. doi: 10.1016/j.jhydrol.2009.08.003
- 913 Gupta, S. K., Tyagi, J., Sharma, G., Jethoo, A. S., & Singh, P. K. (2019). An Event-Based Sediment Yield and  
914 Runoff Modeling Using Soil Moisture Balance/Budgeting (SMB) Method. *Water Resources*  
915 *Management*, 33(11), 3721-3741. doi: 10.1007/s11269-019-02329-1
- 916 Guse, B., Pfannerstill, M., Gafurov, A., Fohrer, N., & Gupta, H. (2016). Demasking the integrated information of  
917 discharge: Advancing sensitivity analysis to consider different hydrological components and their rates  
918 of change. *Water Resources Research*, 52(11), 8724-8743. doi: 10.1002/2016wr018894
- 919 Hamedi, F., Bozorg-Haddad, O., Orouji, H., Fallah-Mehdipour, E., & Loaiciga, H. A. (2016). Nonlinear  
920 Muskingum Model for Flood Routing in Irrigation Canals Using Storage Moving Average. *Journal of*  
921 *Irrigation and Drainage Engineering*, 142(5). doi: 10.1061/(asce)ir.1943-4774.0001000
- 922 Hamilton, A., Hutchinson, D., & Moore, R. (2000). Estimating winter streamflow using conceptual streamflow  
923 model. *Journal of Cold Regions Engineering*, 14(4), 158-175. doi: 10.1061/(ASCE)0887-  
924 381X(2000)14:4(158)
- 925 Hassini, S., & Guo, Y. P. (2017). Derived flood frequency distributions considering individual event hydrograph  
926 shapes. *Journal of Hydrology*, 547, 296-308. doi: 10.1016/j.jhydrol.2017.02.003
- 927 He, R., Zhang, J., Bao, Z., Yan, X., Wang, G., & Liu, C. (2015). Response of runoff to climate change in the Haihe  
928 River basin. *Advances in Water Science*, 26(1), 1-9. doi: 10.14042/j.cnki.32.1309.2015.01.001
- 929 Hood, M. J., Clausen, J. C., & Warner, G. S. (2007). Comparison of stormwater lag times for low impact and  
930 traditional residential development. *Journal of the American Water Resources Association*, 43(4), 1036-  
931 1046. doi: 10.1111/j.1752-1688.2007.00085.x
- 932 Huang, C. C., Wang, G. Q., Zheng, X. G., Yu, J. S., & Xu, X. Y. (2015a). Simple Linear Modeling Approach for  
933 Linking Hydrological Model Parameters to the Physical Features of a River Basin. *Water Resources*  
934 *Management*, 29(9), 3265-3289. doi: 10.1007/s11269-015-0996-9
- 935 Huang, J. B., Wen, J. W., Wang, B., & Zhu, S. J. (2015b). Numerical analysis of the combined rainfall-runoff  
936 process and snowmelt for the Alun River Basin, Heilongjiang, China. *Environmental Earth Sciences*,  
937 74(9), 6929-6941. doi: 10.1007/s12665-015-4694-y
- 938 Jakeman, A. J., & Hornberger, G. M. (1993). How much complexity is warranted in a rainfall-runoff model? *Water*  
939 *Resources Research*, 29(8), 2637-2649. doi: 10.1029/93WR00877
- 940 Knighton, J., White, E., Lennon, E., & Rajan, R. (2014). Development of probability distributions for urban  
941 hydrologic model parameters and a Monte Carlo analysis of model sensitivity. *Hydrological Processes*,  
942 28(19), 5131-5139. doi: 10.1002/hyp.10009

- 943 Knoben, W. J., Freer, J. E., & Woods, R. A. (2019). Inherent benchmark or not? Comparing Nash–Sutcliffe and  
944 Kling–Gupta efficiency scores. *Hydrology and Earth System Sciences*, 23(10), 4323–4331. doi:  
945 10.5194/hess-23-4323-2019
- 946 Kollat, J., Reed, P., & Wagener, T. (2012). When are multiobjective calibration trade - offs in hydrologic models  
947 meaningful? *Water Resources Research*, 48(3). doi: 10.1029/2011WR011534
- 948 Krasnostein, A. L., & Oldham, C. E. (2004). Predicting wetland water storage. *Water Resources Research*, 40(10).  
949 doi: 10.1029/2003wr002899
- 950 Kundzewicz, Z. W., Hirabayashi, Y., & Kanae, S. (2010). River floods in the changing climate—observations and  
951 projections. *Water Resources Management*, 24(11), 2633–2646. doi: 10.1007/s11269-009-9571-6
- 952 Li, J., Liu, C. M., Wang, Z. G., & Liang, K. (2015). Two universal runoff yield models: SCS vs. LCM. *Journal of*  
953 *Geographical Sciences*, 25(3), 311–318. doi: 10.1007/s11442-015-1170-2
- 954 Li, M. Y., Liu, T. X., Duan, L. M., Luo, Y. Y., Ma, L., Wang, Y. X., et al. (2020). Scale transfer and simulation of  
955 the infiltration in chestnut soil in a semi-arid grassland basin. *Ecological Engineering*, 158. doi:  
956 10.1016/j.ecoleng.2020.106045
- 957 Li, M. Y., Liu, T. X., Duan, L. M., Ma, L., Wang, Y. X., Zhou, Y. J., et al. (2021). Hydrologic gradient changes of  
958 soil respiration in typical steppes of Eurasia. *Science of the Total Environment*, 794. doi:  
959 10.1016/j.scitotenv.2021.148684
- 960 Liang, S., Cheng, C., Jia, K., Jiang, B., Liu, Q., Xiao, Z., et al. (2020). The Global LAnd Surface Satellite (GLASS)  
961 products suite. *Bulletin of the American Meteorological Society*. doi: 10.1175/BAMS-D-18-0341.1
- 962 Liang, S., Zhang, X., Xiao, Z., Cheng, J., Liu, Q., & Zhao, X. (2013a). Global LAnd Surface Satellite (GLASS)  
963 products: Algorithms, validation and analysis. *Springer*. doi:  
964 Liang, S. L., Zhao, X., Liu, S. H., Yuan, W. P., Cheng, X., Xiao, Z. Q., et al. (2013b). A long-term Global LAnd  
965 Surface Satellite (GLASS) data-set for environmental studies. *International Journal of Digital Earth*, 6,  
966 5–33. doi: 10.1080/17538947.2013.805262
- 967 Liang, Z. M., Wang, J., Li, B. Q., & Yu, Z. B. (2012). A statistically based runoff-yield model coupling infiltration  
968 excess and saturation excess mechanisms. *Hydrological Processes*, 26(19), 2856–2865. doi:  
969 10.1002/hyp.8357
- 970 Lopes, V. L., & Canfield, H. E. (2004). Effects of watershed representation on runoff and sediment yield modeling.  
971 *Journal of the American Water Resources Association*, 40(2), 311–319. doi: 10.1111/j.1752-  
972 1688.2004.tb01031.x
- 973 Lou, H. Z., Yang, S. T., Hao, F. H., Jiang, L. M., Zhao, C. S., Ren, X. Y., et al. (2019). SMAP, RS-DTVGM, and  
974 in-situ monitoring: Which performs best in presenting the soil moisture in the middle-high latitude frozen  
975 area in the Sanjiang Plain, China? *Journal of Hydrology*, 571, 300–310. doi:  
976 10.1016/j.jhydrol.2018.12.023
- 977 Ma, F., Ye, A. Z., & Duan, Q. Y. (2019). Seasonal drought ensemble predictions based on multiple climate models  
978 in the upper Han River Basin, China. *Climate Dynamics*, 53(12), 7447–7460. doi: 10.1007/s00382-017-  
979 3577-1
- 980 Maniquiz, M. C., Kim, L. H., Lee, S., & Choi, J. (2012). Flow and mass balance analysis of eco-bio infiltration  
981 system. *Frontiers of Environmental Science & Engineering*, 6(5), 612–619. doi: 10.1007/s11783-012-  
982 0448-1
- 983 Melsen, L. A., & Guse, B. (2019). Hydrological Drought Simulations: How Climate and Model Structure Control  
984 Parameter Sensitivity. *Water Resources Research*, 55(12), 10527–10547. doi: 10.1029/2019wr025230
- 985 Metivier, F., Devauchelle, O., Chauvet, H., Lajeunesse, E., Meunier, P., Blanckaert, K., et al. (2016). Geometry of  
986 meandering and braided gravel-bed threads from the Bayanbulak Grassland, Tianshan, P. R. China. *Earth*

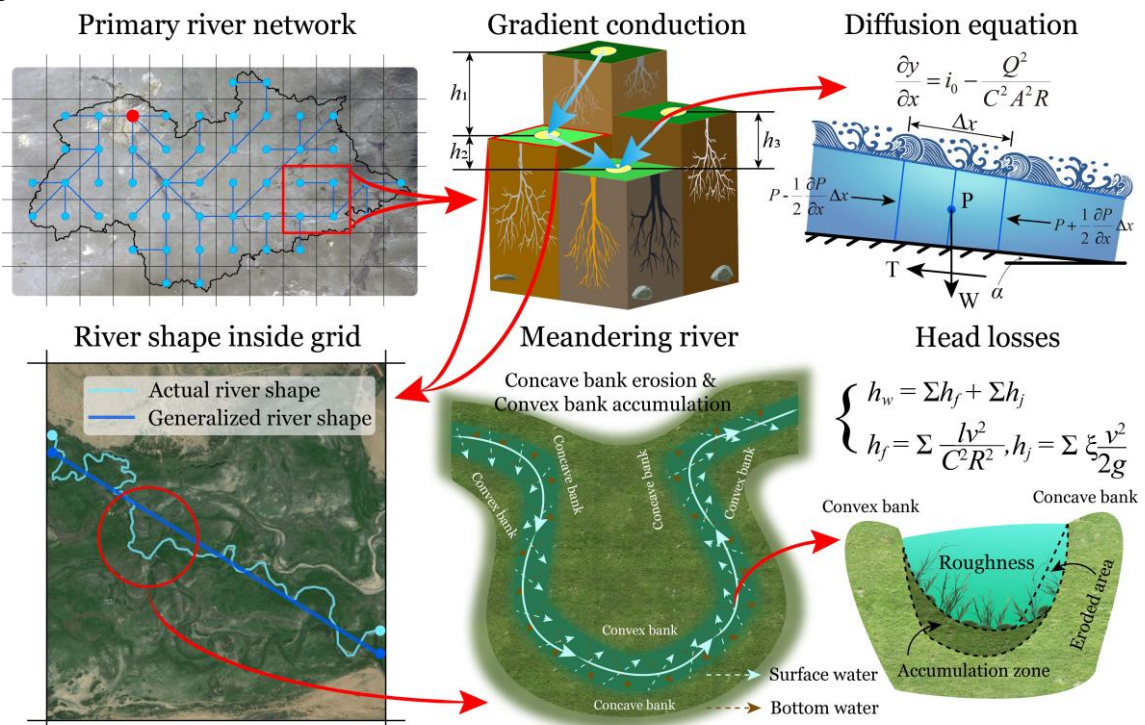
- 987 *Surface Dynamics*, 4(1), 273-283. doi: 10.5194/esurf-4-273-2016
- 988 Minville, M., Brissette, F., & Leconte, R. (2010). Impacts and uncertainty of climate change on water resource  
989 management of the Peribonka River System (Canada). *Journal of Water Resources Planning and*  
990 *Management*, 136(3), 376-385. doi: 10.1061/(ASCE)WR.1943-5452.0000041
- 991 Misirli, F., Gupta, H. V., Sorooshian, S., & Thiemann, M. (2003). Bayesian recursive estimation of parameter and  
992 output uncertainty for watershed models. *Calibration of Watershed Models, Water Sci. Appl. Ser.*, 6, 113-  
993 124. doi: 10.1029/WS006p0113
- 994 Moore, I. D., & Grayson, R. B. (1991). Terrain-based catchment partitioning and runoff prediction using vector  
995 elevation data. *Water Resources Research*, 27(6), 1177-1191. doi: 10.1029/91WR00090
- 996 Moore, R. (2007). The PDM rainfall-runoff model. *Hydrology and Earth System Sciences*, 11(1), 483-499. doi:  
997 10.5194/hess-11-483-2007
- 998 Muzik, I. (1992). Derivation of unit and flood hydrographs using a gis. *Environmental monitoring and assessment*,  
999 23(1-3), 45-56. doi: 10.1007/bf00406951
- 1000 Nash, J. E., & Sutcliffe, J. E. (1970). River flow forecasting through conceptual models. Part 1 - A discussion of  
1001 principles. *Journal of Hydrology*, 10, 282-290. doi: 10.1016/0022-1694(70)90255-6
- 1002 Nourani, V., Baghanam, A. H., Adamowski, J., & Kisi, O. (2014). Applications of hybrid wavelet-Artificial  
1003 Intelligence models in hydrology: A review (vol 514, pg 358, 2014). *Journal of Hydrology*, 517, 1189-  
1004 1189. doi: 10.1016/j.jhydrol.2014.06.024
- 1005 Osborn, H. B., & Lane, L. (1969). Precipitation-runoff relations for very small semiarid rangeland watersheds.  
1006 *Water Resources Research*, 5(2), 419-425. doi: 10.1029/WR005i002p00419
- 1007 Pfannerstill, M., Guse, B., Reusser, D., & Fohrer, N. (2015). Process verification of a hydrological model using a  
1008 temporal parameter sensitivity analysis. *Hydrology and Earth System Sciences*, 19(10), 4365-4376. doi:  
1009 10.5194/hess-19-4365-2015
- 1010 Poiani, K. A., & Johnson, W. C. (1993). A Spatial Simulation Model of Hydrology and Vegetation Dynamics in  
1011 Semi-Permanent Prairie Wetlands. *Ecological applications : a publication of the Ecological Society of*  
1012 *America*, 3(2), 279-293. doi: 10.2307/1941831
- 1013 Qi, W., Zhang, C., Fu, G. T., Sweetapple, C., & Liu, Y. L. (2019). Impact of robustness of hydrological model  
1014 parameters on flood prediction uncertainty. *Journal of Flood Risk Management*, 12. doi:  
1015 10.1111/jfr3.12488
- 1016 Qiu, G. Y., Shi, P. J., & Wang, L. M. (2006). Theoretical analysis of a remotely measurable soil evaporation  
1017 transfer coefficient. *Remote Sensing of Environment*, 101(3), 390-398. doi: 10.1016/j.rse.2006.01.007
- 1018 Reaney, S. M., Bracken, L. J., & Kirkby, M. J. (2014). The importance of surface controls on overland flow  
1019 connectivity in semi-arid environments: results from a numerical experimental approach. *Hydrological*  
1020 *Processes*, 28(4), 2116-2128. doi: 10.1002/hyp.9769
- 1021 Renard, B., Kavetski, D., Leblois, E., Thyer, M., Kuczera, G., & Franks, S. W. (2011). Toward a reliable  
1022 decomposition of predictive uncertainty in hydrological modeling: Characterizing rainfall errors using  
1023 conditional simulation. *Water Resources Research*, 47. doi: 10.1029/2011wr010643
- 1024 Rodell, M., Houser, P. R., Jambor, U., Gottschalek, J., Mitchell, K., Meng, C. J., et al. (2004). The Global Land  
1025 Data Assimilation System. *Bulletin of the American Meteorological Society*, 85(3), 381-394. doi:  
1026 10.1175/BAMS-85-3-381
- 1027 Sang, Y. F. (2013). A review on the applications of wavelet transform in hydrology time series analysis.  
1028 *Atmospheric Research*, 122, 8-15. doi: 10.1016/j.atmosres.2012.11.003
- 1029 Schoups, G., & Nasserli, M. (2021). GRACEfully Closing the Water Balance: A Data-Driven Probabilistic  
1030 Approach Applied to River Basins in Iran. *Water Resources Research*, 57(6). doi:

- 1031 10.1029/2020wr029071
- 1032 Seibert, J. (2000). Multi-criteria calibration of a conceptual runoff model using a genetic algorithm. *Hydrology*  
1033 *and Earth System Sciences*, 4(2), 215-224. doi: 10.5194/hess-4-215-2000
- 1034 Sikorska, A. E., Montanari, A., & Koutsoyiannis, D. (2015). Estimating the Uncertainty of Hydrological  
1035 Predictions through Data-Driven Resampling Techniques. *Journal of Hydrologic Engineering*, 20(1). doi:  
1036 10.1061/(asce)he.1943-5584.0000926
- 1037 Song, C. L., Wang, G. X., Mao, T. X., Dai, J. C., & Yang, D. Q. (2020). Linkage between permafrost distribution  
1038 and river runoff changes across the Arctic and the Tibetan Plateau. *Science China-Earth Sciences*, 63(2),  
1039 292-302. doi: 10.1007/s11430-018-9383-6
- 1040 Song, X. M., Zhan, C. S., & Xia, J. (2012). Integration of a statistical emulator approach with the SCE-UA method  
1041 for parameter optimization of a hydrological model. *Chinese Science Bulletin*, 57(26), 3397-3403. doi:  
1042 10.1007/s11434-012-5305-x
- 1043 Staudt, F., Mullarney, J. C., Pilditch, C. A., & Huhn, K. (2019). Effects of grain-size distribution and shape on  
1044 sediment bed stability, near-bed flow and bed microstructure. *Earth Surface Processes and Landforms*,  
1045 44(5), 1100-1116. doi: 10.1002/esp.4559
- 1046 Strelkoff, T. (1970). Numerical Solution of Saint-Venant Equations. *Journal of the Hydraulics division*, 96(1),  
1047 223-252. doi: doi:10.1061/JYCEAJ.0002262
- 1048 Sun, R. C., Hernandez, F., Liang, X., & Yuan, H. L. (2020). A Calibration Framework for High-Resolution  
1049 Hydrological Models Using a Multiresolution and Heterogeneous Strategy. *Water Resources Research*,  
1050 56(8), 26. doi: 10.1029/2019wr026541
- 1051 Svoray, T., Assouline, S., & Katul, G. (2015). Introduction to a special section on ecohydrology of semiarid  
1052 environments: Confronting mathematical models with ecosystem complexity. *Water Resources Research*,  
1053 51(11), 8677-8683. doi: 10.1002/2015wr018131
- 1054 Tanaka, Y., Matsukura, Y., Batnasan, N., & Tuvshinjargal, D. (2005). Distinct runoff processes in granite and  
1055 sandstone drainage basins near Ulaanbaatar, Mongolia. *Environmental Geology*, 47(5), 640-646. doi:  
1056 10.1007/s00254-004-1189-7
- 1057 Tang, Y., Leon, A. S., & Kavvas, M. L. (2020). Impact of Size and Location of Wetlands on Watershed-Scale  
1058 Flood Control. *Water Resources Management*, 34(5), 1693-1707. doi: 10.1007/s11269-020-02518-3
- 1059 Tang, Y., Reed, P. M., & Kollat, J. B. (2007). Parallelization strategies for rapid and robust evolutionary  
1060 multiobjective optimization in water resources applications. *Advances in Water Resources*, 30(3), 335-  
1061 353. doi: 10.1016/j.advwatres.2006.06.006
- 1062 Tong, R., Parajka, J., Salentinig, A., Pfeil, I., Komma, J., Szeles, B., et al. (2021). The value of ASCAT soil  
1063 moisture and MODIS snow cover data for calibrating a conceptual hydrologic model. *Hydrology and*  
1064 *Earth System Sciences*, 25(3), 1389-1410. doi: 10.5194/hess-25-1389-2021
- 1065 Tung, Y. K. (1985). River Flood Routing by Nonlinear Muskingum Method. *Journal of Hydraulic Engineering*,  
1066 111(12), 1447-1460. doi: doi:10.1061/(ASCE)0733-9429(1985)111:12(1447)
- 1067 Vassova, D. (2013). Comparison of Rainfall-Runoff Models for Design Discharge Assessment in a Small  
1068 Ungauged Catchment. *Soil and Water Research*, 8(1), 26-33. doi: 10.17221/36/2012-swr
- 1069 Wagener, T., & Montanari, A. (2011). Convergence of approaches toward reducing uncertainty in predictions in  
1070 ungauged basins. *Water Resources Research*, 47. doi: 10.1029/2010wr009469
- 1071 Wagener, T., Wheater, H., & Gupta, H. V. (2004). *Rainfall-runoff modelling in gauged and ungauged catchments*:  
1072 World Scientific.
- 1073 Wang, G. T., Chen, S., & Boll, J. (2003). A semianalytical solution of the Saint-Venant equations for channel flood  
1074 routing. *Water Resources Research*, 39(4). doi: 10.1029/2002wr001690

- 1075 Wang, R., Li, R., Li, J., & Hu, C. M. (2014). A hydraulics-based analytical method for artificial water  
1076 replenishment in wetlands by reservoir operation. *Ecological Engineering*, *62*, 71-76. doi:  
1077 10.1016/j.ecoleng.2013.10.026
- 1078 Wendi, D., Merz, B., & Marwan, N. (2019). Assessing Hydrograph Similarity and Rare Runoff Dynamics by  
1079 Cross Recurrence Plots. *Water Resources Research*, *55*(6), 4704-4726. doi: 10.1029/2018wr024111
- 1080 Wu, Y. Y., Huang, L., Zhao, C. W., Chen, M. H., & Ouyang, W. (2021a). Integrating hydrological, landscape  
1081 ecological, and economic assessment during hydropower exploitation in the upper Yangtze River.  
1082 *Science of the Total Environment*, *767*, 12. doi: 10.1016/j.scitotenv.2021.145496
- 1083 Wu, Z. J., Zhang, J. H., Deng, F., Zhang, S., Zhang, D., Xun, L., et al. (2021b). Fusion of GF and MODIS Data  
1084 for Regional-Scale Grassland Community Classification with EVI2 Time-Series and Phenological  
1085 Features. *Remote Sensing*, *13*(5), 19. doi: 10.3390/rs13050835
- 1086 Xiong, L. H., & Guo, S. L. (2004). Effects of the catchment runoff coefficient on the performance of TOPMODEL  
1087 in rainfall-runoff modelling. *Hydrological Processes*, *18*(10), 1823-1836. doi: 10.1002/hyp.1449
- 1088 Xu, H., Ye, M., & Li, J. (2009). The ecological characteristics of the riparian vegetation affected by river  
1089 overflowing disturbance in the lower Tarim River. *Environmental Geology*, *58*(8), 1749-1755. doi:  
1090 10.1007/s00254-008-1674-5
- 1091 Yamanaka, T., & Ma, W. C. (2017). Runoff prediction in a poorly gauged basin using isotope-calibrated models.  
1092 *Journal of Hydrology*, *544*, 567-574. doi: 10.1016/j.jhydrol.2016.12.005
- 1093 Yan, H. X., Sun, N., Fullerton, A., & Baerwalde, M. (2021). Greater vulnerability of snowmelt-fed river thermal  
1094 regimes to a warming climate. *Environmental Research Letters*, *16*(5), 13. doi: 10.1088/1748-  
1095 9326/abf393
- 1096 Yang, H., Piao, S. L., Zeng, Z. Z., Ciais, P., Yin, Y., Friedlingstein, P., et al. (2015). Multicriteria evaluation of  
1097 discharge simulation in Dynamic Global Vegetation Models. *Journal of Geophysical Research-  
1098 Atmospheres*, *120*(15), 7488-7505. doi: 10.1002/2015jd023129
- 1099 Yang, K., He, J., Tang, W. J., Qin, J., & Cheng, C. C. K. (2010). On downward shortwave and longwave radiations  
1100 over high altitude regions: Observation and modeling in the Tibetan Plateau. *Agricultural and Forest  
1101 Meteorology*, *150*(1), 38-46. doi: 10.1016/j.agrformet.2009.08.004
- 1102 Yin, S. Q., Zhu, Z. Y., Wang, L., Liu, B. Y., Xie, Y., Wang, G. N., & Li, Y. S. (2018). Regional soil erosion  
1103 assessment based on a sample survey and geostatistics. *Hydrology and Earth System Sciences*, *22*(3),  
1104 1695-1712. doi: 10.5194/hess-22-1695-2018
- 1105 Yin, X. W., Feng, Q., Zheng, X. J., Zhu, M., Wu, X., Guo, Y., et al. (2021). Spatio-temporal dynamics and eco-  
1106 hydrological controls of water and salt migration within and among different land uses in an oasis-desert  
1107 system. *Science of the Total Environment*, *772*, 12. doi: 10.1016/j.scitotenv.2021.145572
- 1108 Yokoo, Y., & Kazama, S. (2012). Numerical investigations on the relationships between watershed characteristics  
1109 and water balance model parameters: searching for universal relationships among regional relationships.  
1110 *Hydrological Processes*, *26*(6), 843-854. doi: 10.1002/hyp.8299
- 1111 Young, C. C., & Liu, W. C. (2015). Prediction and modelling of rainfall-runoff during typhoon events using a  
1112 physically-based and artificial neural network hybrid model. *Hydrological Sciences Journal-Journal Des  
1113 Sciences Hydrologiques*, *60*(12), 2102-2116. doi: 10.1080/02626667.2014.959446
- 1114 Zha, X. N., Xiong, L. H., Guo, S. L., Kim, J. S., & Liu, D. D. (2020). AR-GARCH with Exogenous Variables as  
1115 a Postprocessing Model for Improving Streamflow Forecasts. *Journal of Hydrologic Engineering*, *25*(8),  
1116 16. doi: 10.1061/(asce)he.1943-5584.0001955
- 1117 Zhang, J. P., Zhang, H., Xiao, H. L., Fang, H. Y., Han, Y. P., & Yu, L. (2021). Effects of rainfall and runoff-yield  
1118 conditions on runoff. *Ain Shams Engineering Journal*, *12*(2), 2111-2116. doi: 10.1016/j.asej.2020.10.010

- 1119 Zhang, L., & Singh, V. P. (2014). Joint and Conditional Probability Distributions of Runoff Depth and Peak  
1120 Discharge Using Entropy Theory. *Journal of Hydrologic Engineering*, 19(6), 1150-1159. doi:  
1121 10.1061/(asce)he.1943-5584.0000906
- 1122 Zocatelli, D., Marra, F., Armon, M., Rinat, Y., Smith, J. A., & Morin, E. (2019). Contrasting rainfall-runoff  
1123 characteristics of floods in desert and Mediterranean basins. *Hydrology and Earth System Sciences*, 23(6),  
1124 2665-2678. doi: 10.5194/hess-23-2665-2019
- 1125
- 1126

1127 Figures



1128

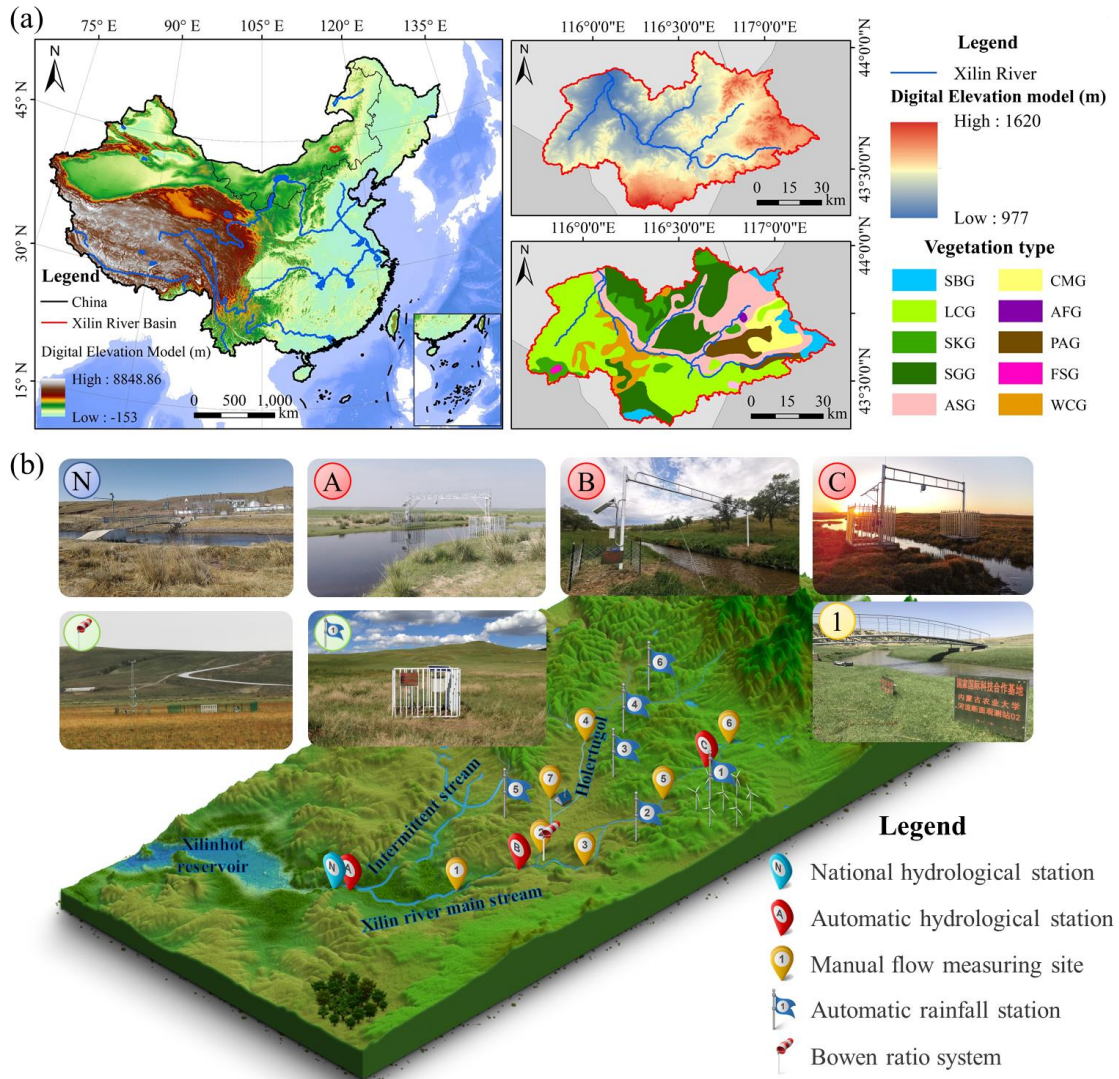
1129

1130

1131

1132

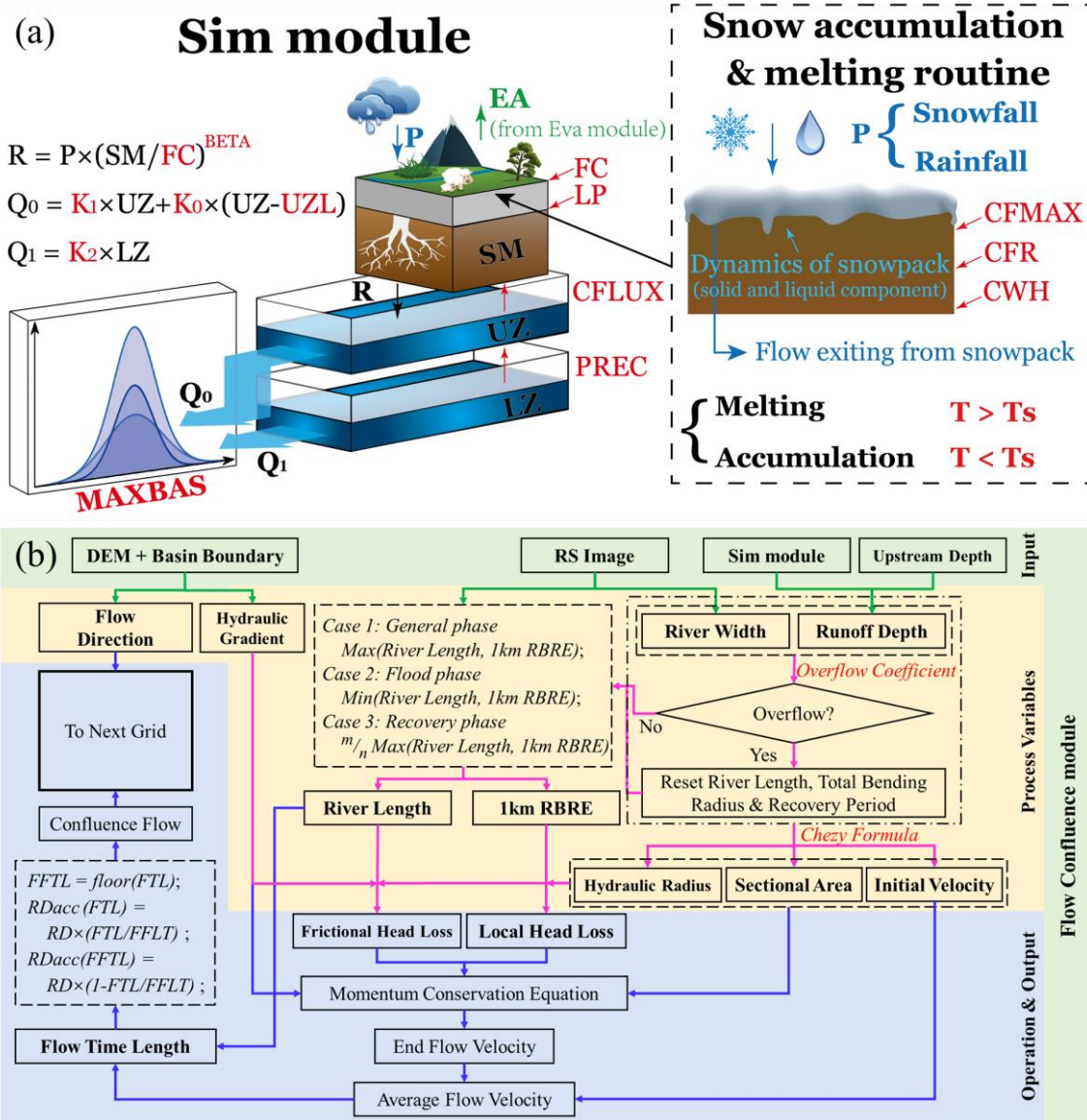
**Figure 1.** Schematic diagram of natural processes such as the flow convergence, actual river lengths, and channel turns of grassland rivers. Note: The river network shown in the figure does not correspond to the real modelled river network resolution.



1133

1134 **Figure 2.** Location, vegetation types (a), topography and stations (b) in the XRB. SBG: *S.*  
 1135 *baicalensis* Roshev. grassland; LCG: *L. chinensis* (Trin.) Tzvel. grassland; SKG: *S. krylovii*  
 1136 Roshev. grassland; SGG: *S. grandis* P.A. Smirn. grassland; ASG: *A. splendens* (Trin.) Nevski  
 1137 grassland; CMG: *C. microphylla* Lam grassland; AFG: *Artemisia frigida* Willd. grassland;  
 1138 PAG: *P. asperata* Mast. grassland; FSG: *Filifolium sibiricum* (L.) Kitam. grassland; and WCG:  
 1139 weed community grassland.

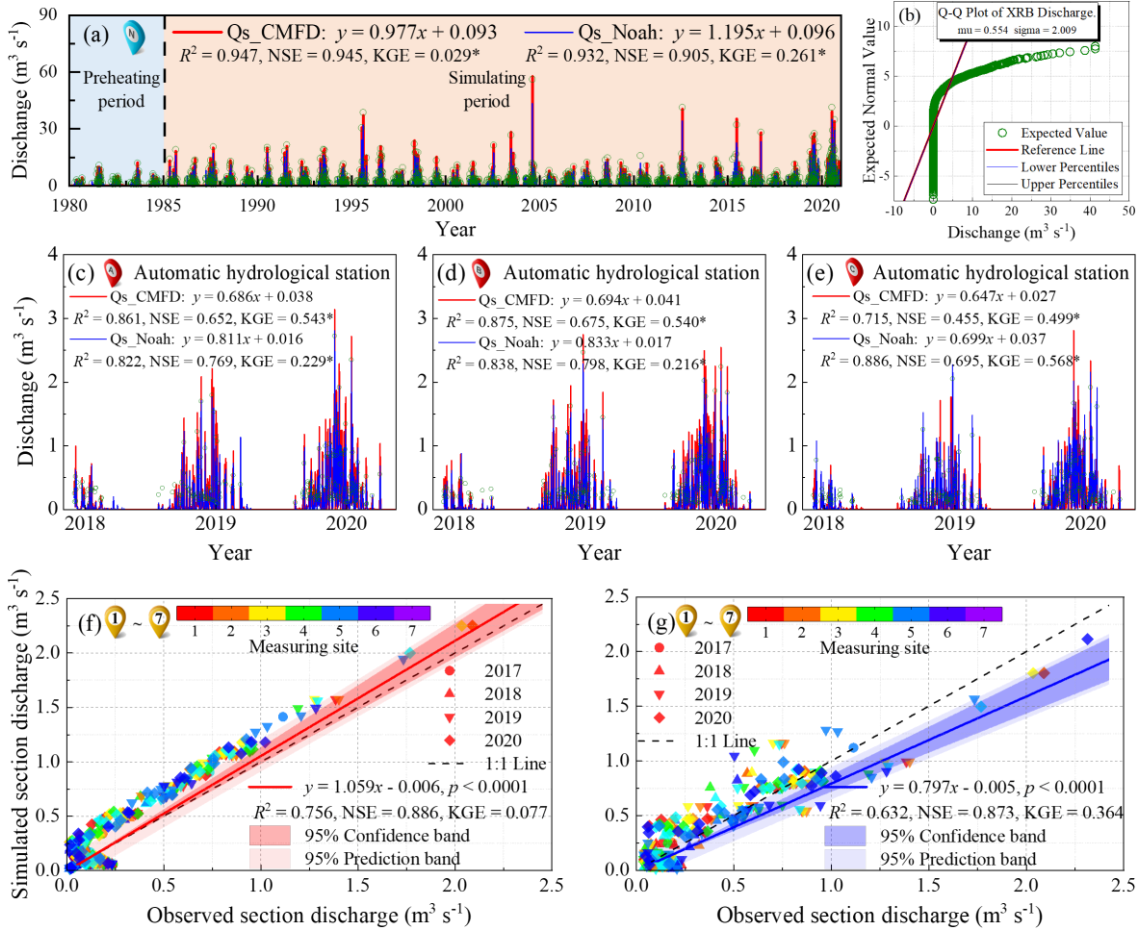
1140



1141

1142 **Figure 3.** (a) Schematic diagram of the MYEH model simulation (Sim) module; (b) schematic  
 1143 diagram of the MYEH model flow confluence (FLC) module. The full names of the variables  
 1144 shown in Figure 3a can be seen in Table 2. DEM: digital elevation model; RS: remote sensing;  
 1145 1-km RBRE: 1-km river bend radius equivalent; FTL: flow time length; FFTL: fixed flow time  
 1146 length; and RDacc: accumulated runoff depth.

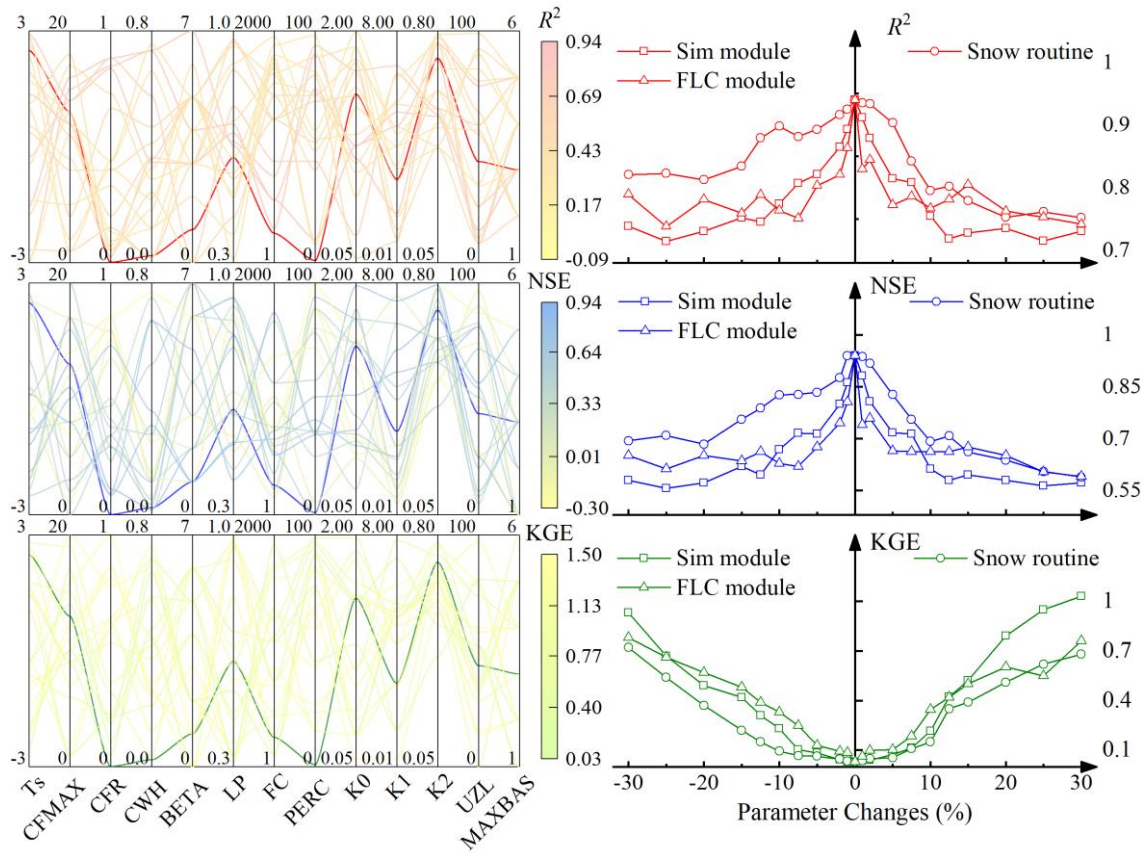
1147



1148

1149 **Figure 4.** (a) Comparison of the simulated and measured daily sectional discharge at a national  
 1150 hydrological station obtained using two meteorologically driven datasets with the MYEH  
 1151 model; (b) Q-Q plot of daily discharge in the XRB; (c-e) comparison of the simulated and  
 1152 measured daily sectional discharge at three automatic hydrological stations using two  
 1153 meteorologically driven datasets with the MYEH model; (f) comparison of the simulated and  
 1154 measured daily sectional discharge at seven measuring sites using the CMFD; and (g)  
 1155 comparison of the simulated and measured daily sectional discharge at seven measuring sites  
 1156 using the GLDAS-NOAH dataset. The green points in (a) to (e) are the values observed at the  
 1157 national hydrological station.

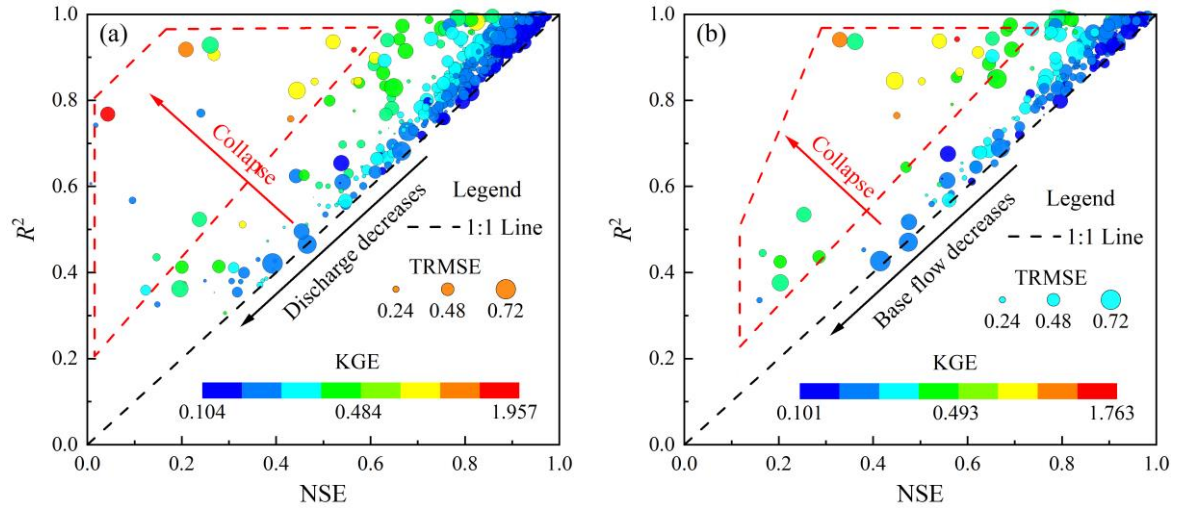
1158



1159

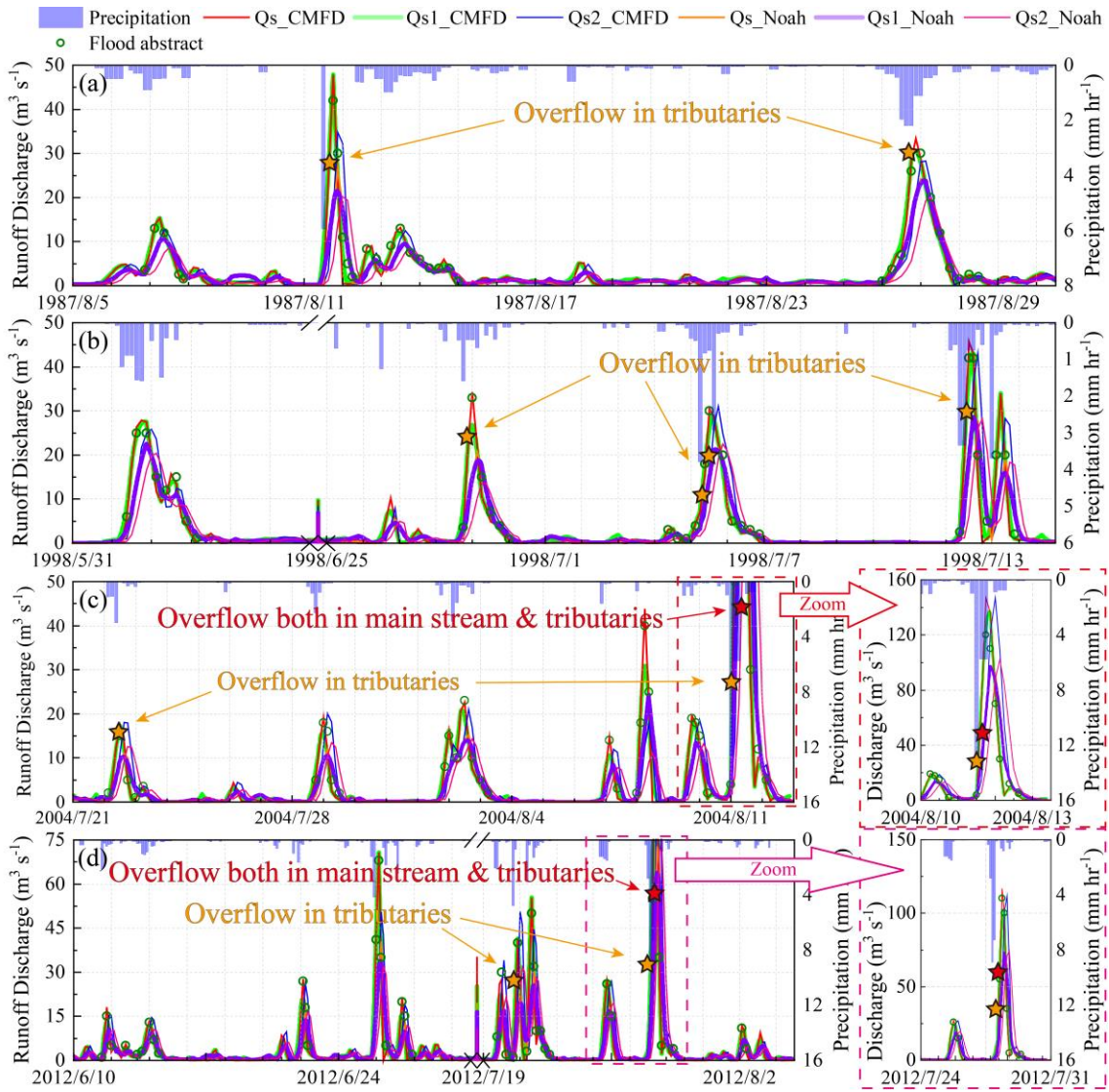
1160 **Figure 5.** Parameter optimization (a-c) and parameter sensitivity analysis (d-f) results obtained  
 1161 for the MYEH model.

1162



1163 **Figure 6.** Comparison of the MYEH model-simulated runoff discharge during the nonfreezing  
 1164 period (a) and base flow during the freezing period (b) in the XRB as determined using the  
 1165 CMFD and GLDAS-NOAH data sources. In this figure, NSE and  $R^2$  are plotted on the X and  
 1166 Y axes, respectively, KGE is plotted in color, and TRMSE is plotted using the size of the  
 1167 markers. The black arrow points in the direction of decreasing flow or base flow. The red arrow  
 1168 indicates the tendency of both data-source simulations to collapse. NSE: Nash-Sutcliffe  
 1169 efficiency; KGE: Kling-Gupta efficiency; and TRMSE: Box-Cox transformed root mean  
 1170 square error.

1171



1172

1173

1174

1175

1176

1177

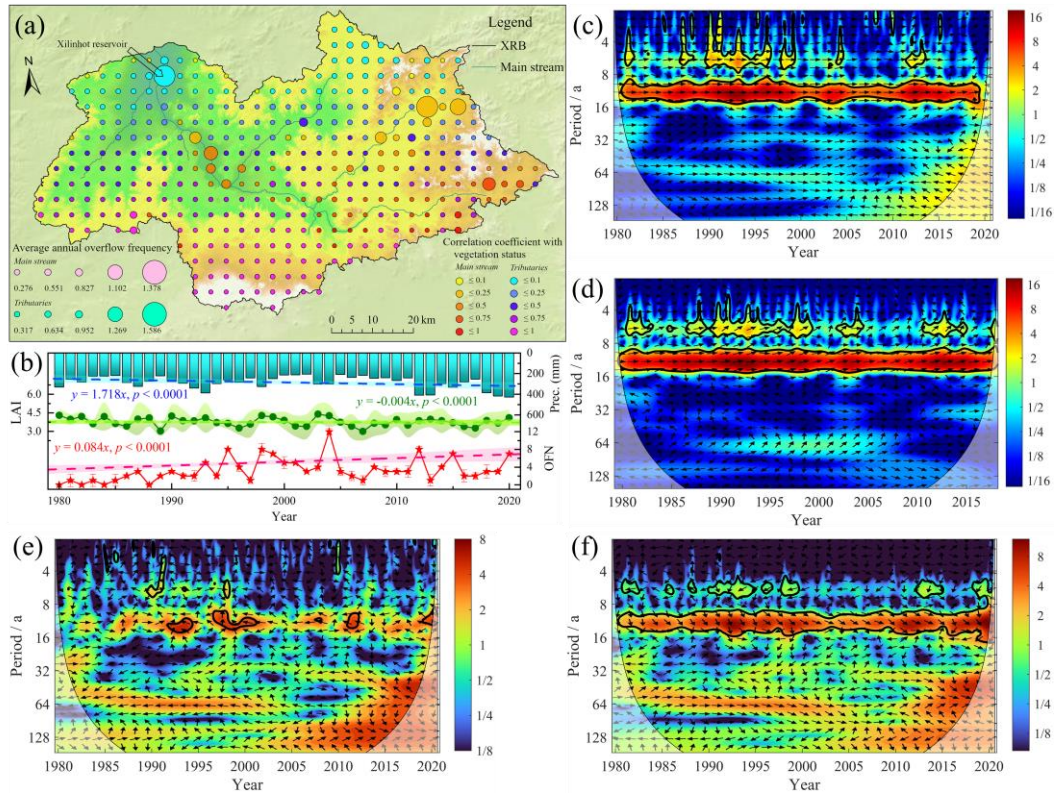
1178

1179

1180

1181

**Figure 7.** Simulations of the 3-hour flood process under three confluence modes using the CMFD and GLDAS-NOAH data sources. Figures 7(a) to 7(d) show monsoon floods in 1987, 1998, 2004 and 2012, respectively. Qs indicates the MYEH model confluence mode (FLC). Qs1 indicates the confluence mode in which the actual river length, river bending and overflow are not considered. Qs2 indicates the confluence mode in which the actual river length and river bending are considered but overflow is not considered. The orange and red stars represent the overflow of tributaries and the overflow of main streams and tributaries in a flood event, respectively.



1182

1183 **Figure 8.** (a) Average annual overflow frequency and the correlation between overflows and  
 1184 vegetation status. (b) Trend analyses of precipitation, LAI, and OFN from 1980 to 2020. (c-f)  
 1185 The cross-wavelet energy spectrum analyses of the OFN with precipitation, LAI, SOI and  
 1186 NINO3.4 SST. The 5% significance level against red noise is shown as a thick contour line.  
 1187 The relative phase relationships are shown as arrows (with in-phase relationships pointing right  
 1188 and anti-phase relationships pointing left).

1189

## Tables

**Table 1.** Information of measurement stations in the XRB.

Name	Collector	Monitoring indicator	Frequency	Data length
National hydrological station	/	Flow discharge	1 day	1964/1/1-2020/12/31
Automatic hydrological station	RQ-30 radar sensor (Sommer GmbH, Austria)	Water level, flow velocity, flow discharge	1 min	2018/8/15-2020/12/31
Bowen ratio system	CR1000 (Campbell Scientific Inc., Logan, UT, USA)	Air temperature*, humidity*, wind speed*, wind direction*, precipitation, total radiation, soil heat flux, etc	1 min	2017/6/15-2020/12/31
Automatic rainfall station	RG600 tilting rain gauge (Global water, USA)	Precipitation	1 min	2016/6/30-2020/12/31
Manual flow measuring site	LS1206B propeller type flow sensor (Nanjing Nanshui Water Technology Company, PRC)	Flow velocity	7 days	Apr. to Oct. from 2017 to 2020

Note: \* represents the monitoring indicator is located at a height of 2,3,5, 5,10 meters.

**Table 2.** Summary of parameters used in the Sim module and FLC module within the MYEH model.

Module	Parameter (Units)	Full name	Range	Module	Parameter (Units)	Full name
	T <sub>s</sub> (°C)	Threshold temperature	-3 to 3		A <sub>G</sub> (km <sup>2</sup> )	Grid area
	CFMAX (mm °C <sup>-1</sup> )	Degree-3-hour factor	0 to 20		W <sub>R</sub> (m)	River width
	CFR (-)	Refreezing factor	0 to 1		L <sub>R</sub> (km)	River length
	CWH (-)	Water holding capacity of snow	0 to 0.8		H <sub>R</sub> (m)	Runoff height
	BETA (-)	Exponential parameter in soil routine	0 to 7		dH (km)	Elevation difference
	LP (-)	Evapotranspiration limit	0.3 to 1		FD (-)	Flow direction
Sim	FC (mm)	Field capacity	1 to 2000	FLC	1km RBRE (degree)	1km river bending radius equivalent
	PERC (mm dt <sup>-1</sup> )	maximum flux from Upper to Lower Zone	0 to 100		v <sub>1</sub> (m dt <sup>-1</sup> )	Initial velocity
	K0 (dt <sup>-1</sup> )	Near surface flow coefficient (ratio)	0.05 to 2		v <sub>2</sub> (m dt <sup>-1</sup> )	End flow velocity
	K1 (dt <sup>-1</sup> )	Upper Zone outflow coefficient (ratio)	0.01 to 8		A <sub>S</sub> (m <sup>2</sup> )	Sectional area
	K2 (dt <sup>-1</sup> )	Lower Zone outflow coefficient (ratio)	0.05 to 0.8		FTL (dt)	Flow time length
	UZL (mm)	Near surface flow threshold	0 to 100		FFTL (dt)	Fixed flow time length
	MAXBAS (dt)	Flow routing coefficient	1 to 6		RD <sub>Acc</sub> (mm)	Accumulated runoff depth

Note: In this table, dt represents the unit time.

**Table 3.** Characteristics of the two meteorological datasets.

Dataset	Version	Date used in study	Temporal resolution
CMFD	01.05.0016	1980.01.01-2018.12.31	3 hours
GLDAS-Noah	V2.0	1980.01.01-2000.12.31	3 hours
GLDAS-Noah	v2.1	2000.01.01-2020.12.31	3 hours

Note: CMFD: China meteorological forcing dataset, in which the temperature, pressure, specific humidity, wind speed, downward shortwave radiation, downward longwave radiation, and precipitation rate data are used in the study. NASA Global Land Data Assimilation System Version 2 (GLDAS-2) has three components: GLDAS-2.0, GLDAS-2.1, and GLDAS-2.2. GLDAS-2.0 is forced entirely with the Princeton meteorological forcing input data and provides a temporally consistent series from 1948 through 2014. GLDAS-2.1 is forced with a combination of model and observation data from 2000 to present.

**Table 4.** Six evaluation value of simulated runoff in XRB using two data sources.

	$R^2$	NSE	KGE	RMSE	BIAS	MAE
CMFD	0.947**	0.946	0.029	0.463	0.003	0.147
GLDAS-Noah	0.932**	0.905	0.262	0.616	0.096	0.191

Note: \*\* indicates that the increasing or decreasing trend is significant at  $\alpha \leq 0.001$ .